การสร้างแบบจำลองพื้นถิ่นโทรโปสเฟียร์สำหรับ REPEAT-PASS SAR INTERFEROMETRY แบบดั้งเดิม พื้นที่ศึกษา: กรุงเทพมหานคร

นายชัยพล กีรติกสิกร

วิทยานิพนธ์นี้เป็นส่วนหนึ่งของการศึกษาตามหลักสูตรปริญญาวิศวกรรมศาสตรดุษฎีบัณฑิต
สาขาวิชาวิศวกรรมสำรวจ ภาควิชาวิศวกรรมสำรวจ
คณะวิศวกรรมศาสตร์ จุฬาลงกรณ์มหาวิทยาลัย
ปีการศึกษา 2554

LOCAL TROPOSPHERIC MODEL FOR CONVENTIONAL REPEAT-PASS SAR INTERFEROMETRY: A CASE STUDY IN BANGKOK

Mr. Chaiyapon Keeratikasikorn

A Dissertation Submitted in Partial Fulfillment of the Requirements
for the Degree of Doctor of Philosophy Program in Geomatic Engineering
Department of Survey Engineering
Faculty of Engineering
Chulalongkorn University
Academic year 2011

Thesis Title	LOCAL TROPOSPHERIC MODEL FOR CONVENTIONAL REPEAT-PASS SAR INTERFEROMETRY: A CASE STUDY IN BANGKOK
By	Mr. Chaiyapon Keeratikasikorn
Field of Study	Geomatic Engineering
Thesis Advisor	Associate Professor Itthi Trisirisatayawong, Ph.D.

Accepted by the Faculty of Engineering, Chulalongkorn University in Partial Fulfillment of the Requirements for the Doctoral Degree

…….. Dean of the Faculty of Engineering
(Associate Professor Boonsom Lerdhirunwong, Ph.D.)

THESIS COMMITTEE

…….. Chairman
(Associate Professor Banjerd Phalakarn, Ph.D.)

…….……. Thesis Advisor
(Associate Professor Itthi Trisirisatayawong, Ph.D.)

…….. Examiner
(Professor Chalermchon Satirapod, Ph.D.)

…….. Examiner
(Thongthit Chayakula, Ph.D.)

…….. External Examiner
(Chaowalit Silapathong, Ph.D.)

ชัยพล กีรติกสิกร. การสร้างแบบจำลองพื้นถิ่นโทรโปสเฟียร์สำหรับ REPEAT-PASS SAR INTERFEROMETRY แบบดั้งเดิม พื้นที่ศึกษา: กรุงเทพมหานคร. (LOCAL TROPOSPHERIC MODEL FOR CONVENTIONAL REPEAT-PASS SAR INTERFEROMETRY: A CASE STUDY IN BANGKOK) อ.ที่ปรึกษาวิทยานิพนธ์หลัก: รศ. ดร.อิทธิ ตริสิริสัตยวงศ์, 57หน้า.

Repeat-pass SAR Interferometry แบบดั้งเดิมเป็นเทคนิคที่ใช้ภาพ SAR 2 ภาพ เพื่อสร้างอินเตอร์เฟอโรแกรมที่ให้ข้อมูลการทรุดตัวของผืนแผ่นดิน ปัจจัยหลักที่ก่อให้เกิด phase error ในอินเตอร์เฟอโรแกรมคือการเปลี่ยนแปลงของปริมาณไอน้ำในชั้นบรรยากาศโทรโปสเฟียร์ ซึ่งเป็นข้อจำกัดที่ทำให้ที่ผ่านมามีการใช้เทคนิคดังกล่าวเฉพาะบริเวณพื้นที่ทะเลทรายหรือบริเวณที่มีความชื้นต่ำเป็นส่วนใหญ่ การศึกษาชิ้นนี้เสนอผลการวิจัยจากการทดลองขจัด phase error จากปริมาณไอน้ำ3 วิธี เพื่อตรวจแก้ความคลาดเคลื่อนของเฟสจากปริมาณไอน้ำในอินเตอร์เฟอโรแกรมที่สร้างจากภาพ TerraSAR-X ที่ครอบคลุมพื้นที่กรุงเทพมหานครฝั่งตะวันออก วิธีการที่หนึ่งสร้างข้อมูล wet delay ที่ได้จากข้อมูลปริมาณไอน้ำของดาวเทียม MODIS แล้วนำมาตรวจแก้ค่าเฟสในอินเตอร์เฟอโรแกรมโดยตรง วิธีการที่สองนำเอาข้อมูลทางอุตุนิยมมาสอบเทียบ เพื่อปรับแก้ค่า wet delay ก่อนนำไปตรวจแก้ค่าเฟสในอินเตอร์เฟอโรแกรม วิธีการที่สามเป็นการปรับปรุงวิธีการที่สองโดยสร้างแบบจำลอง time-shifted linear fit model เพื่อคำนวณค่า wet delay ที่เกิดขึ้น ณ ขณะเวลาที่บันทึกภาพ TerraSAR-X ซึ่งเกิดขึ้นก่อนเวลาบันทึกภาพ MODIS ประมาณ 5 ชั่วโมง จากผลการศึกษาพบว่า วิธีการที่สามซึ่งนำเอาข้อเท็จจริงที่ว่าปริมาณไอน้ำในชั้นบรรยากาศแปรตามเวลาเข้าไปร่วมกำหนดแบบจำลองให้ค่าตรวจแก้ที่ดีที่สุด ตามด้วยวิธีการที่สองที่ให้ผลลัพธ์ดีกว่าวิธีการที่หนึ่งซึ่งนำข้อมูลปริมาณไอน้ำของดาวเทียม MODIS มาใช้โดยตรง ทั้งนี้ ความถูกต้องจากกระบวนการสอบเทียบสามารถเพิ่มขึ้นได้หากมีการใช้ GPS ร่วมในกระบวนสร้างแบบจำลอง รวมถึงมีจำนวนสถานี GPS และอุตุนิยมที่มากขึ้น

ภาควิชา วิศวกรรมสำรวจ ลายมือชื่อนิสิต .....

สาขาวิชา วิศวกรรมสำรวจ ลายมือชื่อ อ.ที่ปรึกษาวิทยานิพนธ์หลัก .....

ปีการศึกษา 2554 .

4971867421 : MAJOR SURVEY ENGINEERING
KEYWORDS : D-InSAR / Saastamoinen model / MODIS / Zenith wet delay

CHAIYAPON KEERATIKASIKORN: LOCAL TROPOSPHERIC MODEL FOR CONVENTIONAL REPEAT-PASS SAR INTERFEROMETRY: A CASE STUDY IN BANGKOK. ADVISOR: ASSOC.PROF. ITTHI TRISIRISATAYAWONG, Ph.D., 57 pp.

Repeat-pass SAR Interferometry is a technique which produces an 'interferogram' giving earth surface deformation data. A major source of phase errors in interferogram is heterogeneous phase delay caused mainly by variation of water vapors in troposphere, which is a factor limiting applications of DInSAR mainly to desert or arid areas. This paper presented study results of three methods to correct atmospheric phase errors from water vapor in interferograms formed by TerraSAR-X images covered the south-eastern part of Bangkok metropolitan. The first method was the use of wet delay derived directly from MODIS precipitable water vapor product to correct the phase error in the interferograms. The second method employed ground-based meteorological data to calibrate MODIS PWV before computing phase delays. The third method improved the second method by estimating the expected MODIS PWV value at the time of the TerraSAR-X image acquisitions which over the Bangkok test area was 5 hour earlier than that of MODIS. The time-shifted linear fit model along with the IDW interpolation was used to estimate more realistic phase delays over entire imaging area. From the study, this time-corrected method provided best results while the second method also achieved a significantly better result than those obtained from direct use of MODIS PWV data. However, the accuracy of the calibration process should be further improved if GPS were integrated in the model and more GPS and ground meteorological stations are available.

Department : Survey Engineering Student's Signature .....
Field of Study : Survey Engineering Advisor's Signature .....
Academic Year : 2011

ACKNOWLEDGEMENTS

First of all, I would like to thank to my advisor, Assoc. Itthi Trisirisatayawong for his guidance and criticism throughout my PhD program and also spending his valuable time commenting on the thesis. I am also thankful to Prof. Chalermchon Satirapod for his advises and contributiom of MATLAB code on the Saastamoinen model which saved a lot of time at the beginning process. I am also grateful to all other examiners, Assoc. Banjerd Phalakarn, Dr. Chaowalit Silapathong and Dr. Thongthit Chayakula for useful comments on the thesis.

TerraSAR-X images used in this study is provided by DLR through a Thailand-EU joint research: Earth Observation Technologies for Thailand: Environmental Change Detection and Investigation (GEO2TECDI) program. MODIS data are freely downloaded from http://modis.gsfc.nasa.gov/; SRTM DEM is freely downloaded from http://www2.jpl.nasa.gov/srtm/cbanddataproducts.html. The authors would like to thank Meteorological Department of Thailand for making the ground meteorological data available for our study. Also, I owe to Survey engineering department which provided purchased license on SARScape 4.0, without the program and processing tools, this thesis could not be done.

There are many people and colleagues at Chulalongkorn University to thank individually for their help and support. Firstly, Anuphao Aobpaet, who always provides me with strong encouragement and brought me along to study InSAR at the University of Alaska, I am grateful to that. Thanks to Arun Bureerak for helping parts of my paper editing and Panuwat Angkasurak for the pre-processing of MODIS data.

Finally, my most appreciation goes to my family, my parents and my younger brother for supporting my seemingly endless education.

CONTENTS

Page

LIST OF TABLES

LIST OF FIGURES

LIST OF ABBREVIATIONS

Abbreviation	
DEM	Digital Elevation Model
DInSAR	Differential Interferometric Synthetic Aperture Radar
ERS	European Remote Sensing satellite
GPS	Global Positioning System
IDW	Inverse Distance Weighting
InSAR	Interferometric SAR
MODIS	Moderate Resolution Imaging Spectroradiometer
NASA	National Aeronautics and Space Administration
PWV	Percipitable Water Vapor
SAR	Synthetic Aperture Radar
SIR-C/X	Shuttle Imaging Radar satellite
SLC	Single Look Complex
SRTM	Shuttle Radar Topography Mission
ZWD	Zenith Wet Delay

CHAPTER I

INTRODUCTION

1.1 Background

Differential Interferometric Synthetic Aperture Radar (DInSAR) is a technique which produces an 'interferogram', an image of phase differences between two SAR images acquired with same viewing geometry over the same region. An advantage of this technique is that it can provide a geographically comprehensive map of the deformation, with a sampling rate far denser than traditional ground surveys e.g. spirit-leveling or Global Positioning System (GPS) (Galloway & Hoffman, 2007). For each pixel in the interferogram, the phase difference (ϕ_{int}) is the sum of contributions phases induced by ground surface displacement between tow SAR image acquisitions (ϕ_{dis}), topography (ϕ_{topo}), difference in atmospheric conditions (ϕ_{atm}), baseline error from imperfect knowledge of orbital or trajectory information (ϕ_{orb}), and noise (ϕ_{noise}), as stated in eq.1

$$\phi_{\text{int}} = \phi_{dis} + \phi_{topo} + \phi_{atm} + \phi_{orb} + \phi_{noise} \qquad (1)$$

In most geophysical applications, the signal of interest is ϕ_{dis}.; various techniques are employed to remove other phase terms from the interferogram. The baseline error manifests itself as long wavelength stripes over the interferogram which could be easily detected and removed. Variability in backscattering of radar pulses, system noise and mis-registration results in noise term. In case the application is to detect ground motion, the topographic phase term can be estimated from available Digital Elevation Model (DEM) and removed. Assuming that the wavelength of signal of interest is large enough so that ϕ_{noise} is uncorrelated over the same distance, a common technique to improve signal-to-noise ratio is to multilook or averaging the interferogram with a window (such as 5x5) comparatively small to signal wavelength. Within the averaging window, the signal remains the same while noise tends to cancel out and decreases.

1.2 Problem

However, it is known that a major source of uncertainty is formed by the atmospheric signal (Hanssen, 2001). The atmospheric phase term is introduced into the interferogram because of the change in the refractive index of the atmosphere between two acquisitions. Though the atmospheric phase delay depends on several atmospheric factors, Zebker *et al.* (1997) concluded those atmospheric *water vapors* are by far the dominant error source in repeat-pass SAR interferometry. For temporal variation, it is known that water vapor values are temporally uncorrelated when their temporal interval is greater than 1 day (Emardson *et al*., 2003), or even over periods of a few hours, particularly in mountainous areas where air is forced to rise over, or

flow around, thereby inducing local overturning and condensation effects at the kilometer scale (Miranda, 1990; Miranda and James, 1992; Webley *et al*., 2002). The spatial scale of water vapor variability is on kilometer scale (Hanssen *et al*. 1999), while in Li *et al.* (2005) it is observed that the atmospheric "ripples" with a characteristic wavelength of 4-12 km. Thus it is correlated within the wavelength of ground displacement and so cannot be removed by any filtering without corrupting the geophysical signal of interest. This is a major problem of 2-pass DInSAR technique and has limited its applications mainly to deserts or arid area. As applications of 2-pass DInSAR usually involves strong signal such as co-seismic motion or volcano eruption, atmospheric phase term can be safely assumed to be small and neglected. However, in tropical areas this assumption is less valid and there is a need the atmospheric phase term is estimated and removed.

1.3 Approach

In the same fashion as DEM is utilized to estimate topographic phase term, external data source is required to estimate the atmospheric phase term. Currently, atmospheric water vapor amount has been continuously measured with the two National Aeronautics and Space Administration (NASA) MODIS instruments. The near-IR water vapor products provided by the Moderate Resolution Imaging Spectroradiometer (MODIS) have a spatial resolution of 1 km × 1 km (at nadir). Even though MODIS data is one of solutions for atmospheric water vapor variation compensation, there is still an important technical problem. As reported by Gao and Kaufman (2003), uncertainties in the surface spectral reflectance, sensor calibration, haze, undetected clouds are estimated to be 5-10% and errors can be up to 14% under hazy conditions. The main reason is that MODIS water vapor amounts are derived from the transmittances based on theoretical calculations and using look-up table procedures. However, atmospheric water vapor has very different absorption coefficients over the band pass of 3 different MODIS channels (Gao and Kaufman, 2003); such that a mean water vapor value is obtained instead and this resulting in water vapor derivation errors, implying that the calibration of MODIS water vapor data is needed before being applied to correct InSAR atmospheric effects.

Li *et al.* (2003a) first presented some results of using MODIS Percipitable Water Vapor (PWV) data to correct atmospheric effects on InSAR over Mt. Etna. The results showed that there were more pixels closer to zero in an unwrapped image with MODIS correction, implied the MODIS correction was effective. Li *et al*. (2005) proposed an integration of MODIS-PWV data and GPS for InSAR atmospheric correction over the Long Beach-Santa Ana basin, where the GPS data are mainly used to calibrate the MODIS-PWV data. The result showed that phase variation of the unwrapped interferogram decreased from 2.48 radians before correction to 1.47 radians after correction. While these results from GPS were encouraging, Qu *et al.* (2008) reported that the zenith delays calculated using ground meteorological data were in accordance with the GPS observations. It has higher temporal resolution and a better accuracy in term of calculating the zenith delay than MODIS-PWV data since being ground observation the presence of clouds or traveling medium has no effect. This research employs ground-based meteorological data to calibrate MODIS-PWV.

1.4 Framework

This research focused on interferogram the methodologies to reduce phase error resulting from water vapor content in the atmosphere. MODIS water vapor content data was employed to derive phase correction while ground-based meteorological data were used to calibrate MODIS data. Test site isthe south-eastern part of Bangkok metropolitan covered by a scene of TerraSAR-X data of 50 km x 30 km.

Based on the above background information, two research questions were formulated:

1) Is the Zenith Wet Delay (ZWD) computed from the Saastamoinen model comparable with the ones acquired from MODIS? If calibrated, the water vapor data should have more accurate values (locally) which bring to better correction results?

2) If the time-difference aspect is brought into consideration, will there be an improvement on the model?

1.5 Objective

Main objective of this thesis was to create a local atmospheric correction model using ground-base meteorological data and MODIS water vapor data.

1.6 Outline

Chapter 2 describes an overview of radar interferometry including Synthetic Aperture Radar (SAR) theory and its interferometric processing such as the theory of 2-pass DInSAR. Parameter estimation of InSAR followed by the theory of atmospheric delays induced in SAR interferogram were presented along with MODIS water vapor data characteristics. Review of atmospheric correction methods focusing on the use of MODIS water vapor correction. Theory on interpolation methods used in this research was also presented.

Chapter 3 describes research methodology showing procedures of three methods to estimate atmospheric phase terms in which details of SAR test images, selection criteria and the formation of interferograms were also presented. The first method was to use MODIS-PWV directly to compute the atmospheric phase as in Saastamoinen model. This served as base case upon which the next two methods would measure against. In second method, meteorological data was employed to calibrate MODIS-PWV before phase computation. Over the test area, the acquisition time of MODIS was 5 hours later than that of TerraSAR-X, the water vapor condition could differ significantly. Third method was an attempt to further improve the second method by estimating the expected MODIS value (acquired around 11 a.m. local time) at the time of the SAR image acquisitions (around 6 a.m.).

Chapter 4 presents results and discussions of the results showing the regression of the ZWD between Saastamoinen model and MODIS data. The comparisons of MODIS water vapor products for correcting atmospheric-induced phase SAR interferogram in three different calibration scenarios were presented. Assessment of the accuracy of each scenario was validated through inter-comparisons using histogram of the data sets.

Chapter 5 presents the main findings and conclusion of the study including the main contributions of this research which is the time-shift linear model, along with the recommendations for future research.

CHAPTER II

LITERATURE REVIEW

2.1 Interferometric SAR (InSAR)

2.1.1 InSAR principle

InSAR rests on a foundation of classical electromagnetic theory and radar-engineering principles (Dzurisin, 2007). It is based on the combination of two radar images, allowing either the retrieval of a Digital Elevation Model (DEM), a digital map of the local topography (InSAR), or the detection of the ground deformations that occurred between the two acquisitions (Raucoules, 2007). The phases of images at the same location with a difference of time (e.g., SAR images acquired at two distinct times) can be compared after proper image registration. The resulting difference of phases is a new kind of image called an *interferogram* which has an interference pattern of *fringes* that containing all the information on relative geometry (Massonnet et al., 1998).

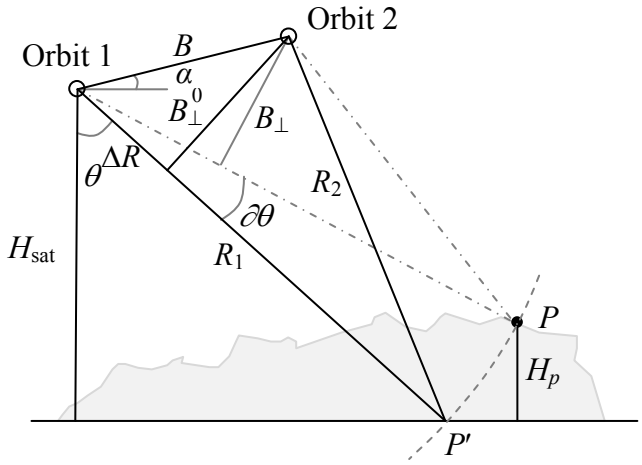

Figure 2.1 InSAR geometry. (Hanssen, 2001)

2.1.2 InSAR geometry

The estimation of topography had been the main focus for the early applications of radar interferometry, yielding elevation accuracies comparable with optical methods (Hanssen, 2001). Using the configuration sketched in figure 2.1, it is able to derive the geometrical relationships between the two observations and obtain topographic height estimates. The distance between the two sensors, measured perpendicular to the look direction, is referred to as the *perpendicular baseline* $B_\perp$. However, the required accuracy for measuring the distance differences between sensors and resolution cell is in the mm-range. As the ranging information (ΔR) determined by the range resolution is three orders of magnitude worse (Hanssen, 2001), it is not applicable for this type of accurate observations. The combination with

phase observations of the received echo provides the solution for this problem. From Hanssen (2001), the relationship between the height H_p above the reference body and the phase difference ϕ_p:

$$H_p = -\frac{\lambda R_{1p} \sin\theta_p^0}{4\pi B_{\perp,p}^0} \partial\phi_p \tag{2}$$

Where perpendicular baseline $B_\perp$ is defined by

$$B_{\perp,p}^0 = B\cos(\theta_p^0 - \alpha) \tag{3}$$

From figure 2.1, the initial value θ^0_p is found for an arbitrary reference surface (e.g., an ellipsoid). A recursive scheme is used to find new values for θ_p at a specific height above this reference surface. Inserting $\phi_p = 2\pi$ in eq. (x) yields the *height ambiguity (H_A)*, the height difference corresponding with a 2π phase shift:

$$H_A = \left| \frac{\lambda R_{1p} \sin\theta_p^0}{2B_{\perp,p}^0} \right| \tag{4}$$

2.1.3 Differential InSAR (D-InSAR)

Repeat-pass SAR interferometry can be used for the measurement of ground deformation. If there is just a ground deformation without distortion of the pixel due to spatial separation (zero-baseline orbit) along the range direction or the line of sight (LOS) between the radar and the target. Then, a phase shift ϕ_{def} due to deformation is defined by (Zhou *et al.*, 2009)

$$\phi_{def} = \frac{4\pi}{\lambda} D \tag{5}$$

The deformation D represents the one-dimensional motion towards the radar therefore, translates directly as a phase shift ϕ_{def} to the interferometric image. Unfortunately, it is often not possible to maneuver the satellite in a zero-baseline orbit. A problem in this application is that, for an effective baseline larger than zero, the deformation signal is always mixed with topographic signal (Hanssen, 2001). Theoretically, the measured interferometric phase ϕ_p is the combination of three different phase terms; the phase term due to reference body, deformation, and topography. When the reference phase ϑp is defined by

$$\vartheta_p = \frac{4\pi}{\lambda} B\sin(\theta_p^0 - \alpha) \tag{6}$$

Using H_p from equation (1), the measured phase ϕ_{p} is defined by

$$\phi_p = \frac{4\pi}{\lambda}(B\sin(\theta_p^0 - \alpha) - D_p - \frac{B_{\perp,p}^0}{R_1 \sin\theta^0} H_p) \quad (7)$$

By subtracting the phase term due to reference body ϑp and topography H_p, then we are left with a topography-removed interferogram that contains only the effects of surface deformation D_p. The method aims at the measurement of ground deformation using repeat-pass interferometry when the non-zero baselines interferogam exists. SAR interferometry follows this kind of technique is specifically called *Differential SAR Inteferometry (D-InSAR)*.

2.2 Parameter Estimation

Radar interferometry can be regarded as a parameter estimation problem, and can be used for the recovery of geophysical parameters (Hanssen, 2001). Theoretically in differential SAR interferometry (D-InSAR), subtracting the unwrapped topographic pair from the deformation pair yields the differential interferogram, which should ideally reflect only deformation signal. In reality, the effects due to stereo topography, base line shift, atmosphere, change of the ground surface or system noise, usually left some residual phase errors. Therefore as shown in eq.1, the phase of a differential interferogram (ϕ_{int}) is the combination of the LOS displacement phase (ϕ_{dis}), the disturbing terms due to decorrelation noise (ϕ_{noise}) and the atmospheric distortion phase (ϕ_{atm}) couple with residual terms caused by topography (ϕ_{topo}) and orbital data (ϕ_{orb}) which also affect the differential interferograms as additional sources of disturbance (Raucoules, 2007). In case that the atmospheric distortion phase (ϕ_{atm}) is the goal of the study. It is expected to be measurable from the differential interferogram if all the other terms are removed.

2.2.1 Orbital phase error

The orbital phase error (ϕ_{orb}) is usually manifested as long-wavelength gradients in the interferogram and can be corrected using tie-points (Hanssen, 2001). However, the availability of precise orbital tracking devices will maintain the accuracy of the interferometric baseline. For ERS-1/2 data, the flat-Earth-like component of $\phi_{orb\text{-}res}$ can usually be assumed as quadratic with the distance among any couple of pixels considered within a full ERS scene interferogram. This behavior allows one to correct the effect by estimating and removing a low-order phase polynomial from a differential interferogram (Raucoules, 2007).

2.2.2 Topographic phase residuals

The topographic phase residuals ($\phi_{topo\text{-}res}$) are any errors from DEM which remain in the topography-removed interferogram. For deformation monitoring, recommendations are as followed (Ferretti *et al*., 2007), select either ascending or descending passes, depending on which will avoid foreshortening in the area of interest. Select those image pairs with the smallest perpendicular baseline in the required range of dates. In fact, the smaller the baseline, the smaller the topography contribution to the interferometric phase. As a consequence, a less precise DEM will be required for the topography subtraction. For example, a 30m error in the DEM

would result in 3 residual fringes in a topography removed interferogram if $h_{2\pi}$ equals 10 m, but only one-third of a fringe if $h_{2\pi}$ equals 90 m (Dzurisin, 2007).

2.2.3 Phase noise

Two types of decorrelation contribute to the phase noise (ϕ_{noise}) which affecting the differential interferometric phase; geometrical decorrelation and temporal decorrelation (Raucoules, 2007). To lessen the geometrical decorrelation effects, it is necessary to select interferometric pairs with a short perpendicular baseline$B_{\perp}$, since the smaller the baseline is, the higher the expected coherence. For temporal decorrelation, it is recommended to choose images acquired within a short period of time to maintain high coherence within the interferogram. Area with high stability e.g. urban area is usually the only type of land surface that can be monitored. Also, a suitable coherence value has often been detected by comparing images at the same time during the year usually winter to winter data is best, when there is the least amount of vegetation on the ground (Ferretti et al., 2007).

2.2.4 Deformation signal

In a differential interferogram, each fringe to the next corresponds to a phase change of 2π. The total number of fringes can be converted to displacement value (the projections along the LOS) by multiplying by $\lambda/2$, where λ is the wavelength of the radar (Zhou *et al*., 2009). Fringe patterns that correspond to a symmetric source are not circular because the radar is side-looking, which means they are more closely spaced where the displacements are upward and toward the radar or downward and away (Dzurisin *et al*., 2007). Hanssen (2001) concluded that, to evaluate the feasibility of radar interferometry for a specific application e.g. subsidence monitoring, especially regarding the influence of atmospheric signal in the data, it is necessary to compare the scale characteristics of the deformation phenomena with those of the atmospheric signal. If the deformation signal is stronger than the atmospheric signal, this implied that the deformation signal is detectable.

2.2.5 Atmospheric signal

A major source of uncertainty is formed by the atmospheric signal (ϕ_a) (Hanssen, 2001), since the effects are spatially correlated but, uncorrelated in time, which means, the corresponding phase terms are spatially correlated at the same location within a single interferogram but, varies from one image to the other (Hanssen, 1996). Typical mid-latitude profiles of temperature and ion density are given in figure 2.2.

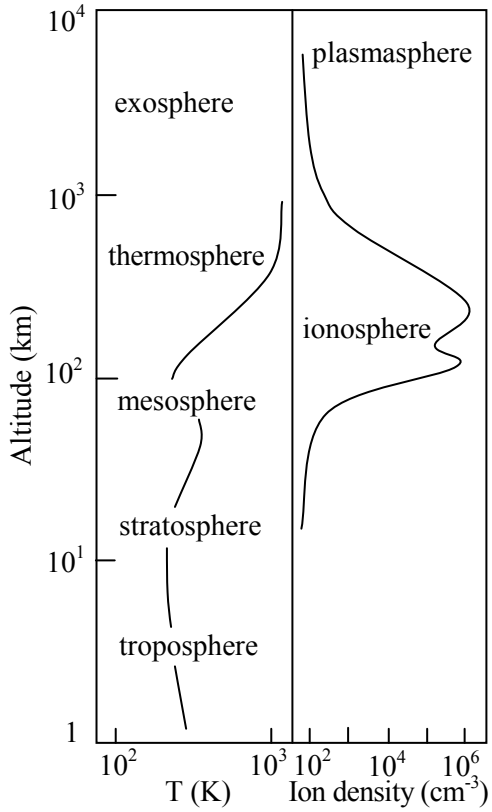

Figure 2.2 Typical atmospheric mid-latitude profiles (Rees, 1989; Li, 2005).

The bottom layer, where the air temperature decreases with altitude, is known as the troposphere. The troposphere contains 80% of the atmosphere's mass (Mason *et al.*, 2001; Li, 2005), and contains 99% of the atmosphere's water vapor (Mocker, 1995; Li, 2005). From the study of Hanssen (2001), he concluded that in case of *troposphere*, phase shift caused by atmospheric refraction can lead to additional phase delay in the interferoram; on the other hand, additional phase advance will occur in case of *ionosphere*. However, since the sensitivity of the instrument (InSAR) depends on phase difference, a phase advance in the master image gives the same result as a phase delay in the slave image. Therefore, it is impossible to distinguish between phase delay and phase advance based solely on a single interferometric pair (Hanssen, 2001).

Spatial charcteristic of ionospheric effect on SAR interferogram have been observed by Price and Sandwell (1998) who found that regional atmospheric effects corresponding to long-wavelength ionospheric perturbations manifest themselves as a planar phase trend in an interferogram. Tarayre and Massonnet (1996a) concluded that this type of homogeneous atmospheric fringe pattern is similar to a fringe pattern due to an orbital error and it is removed when correcting the orbits. Hanssen (1996) found that the spatial extensions of TID are mostly larger than 30 km, and due to this relatively long extension, it is expected that the effect of ionospheric disturbances to be almost linear for ERS quarter scenes. In term of magnitude, Massonnet and Feigl (1995) found that the influence of Travelling Ionospheric Disturbances (TID) on the

propagation of electromagnetic waves is dependent of the frequency of the signal and has been observed up to 2.8 cm for C-band radar. Tarayre and Massonnet (1996a) found that the irregularities of the F-layer can reach 1.5 fringes in C band. Simulations done by Tarayre and Massonnet (1996b) show that (TID) creates a 1.1 cm phase shift in the standard ionosphere with a sinusoidal shape. Wegmuller (2006) found that ionospheric phase effects up to 4π were observed for the affected areas.

However, *Tropospheric disturbances* are more common to occur, even on sub kilometer scale (Tarayre and Massonnet, 1994). Massonnet and Feigl (1995) reported the *first speculations* on the contamination of atmospheric origin in the interferograms using ERS data. Goldstein (1995) found that interferograms acquired over the Mojave Desert in California by SIR-C contained oneway travel errors, expressed as distance, of 0.3 cm rms spread throughout the radar image. These errors exhibited the characteristic Kolmogorov 8/3 power law spectrum associated with turbulence. Hanssen *et al.*, (1996) has been observed smooth changes of the order of 0.3 fringes on ERS interferograms. Under unstable conditions, the refractive index can change more quickly leading to artifacts up to 2 or 3 fringes. Artifacts due to growing cumulus have been observed on the Landers site. Hanssen *et al.*, (1999) reported that the variations of water vapor in Earth's atmosphere are common on a 1-km spatial scale and far more spatially variable than the hydrostatic and ionospheric delays.

Price and Sandwell (1998) reported that short-wavelength atmospheric artifacts typically have length scales on the order of 5-10 km and can cause as much as 10 cm of excess two-way path length (3 interferogram fringes). Hanssen *et al.*, (1996) experimented tropospheric effects on two-pass interferometry using ERS1/2 tandem data to find the relationship between tropospheric parameters and relative interferometric phase changes, results as followed: with a difference of 5 HPa (pressure changes), represents a corresponding phase shift of 0.4 phase cycle and will be visible as a *linear trend* in the interferogram. Also, to assume that temperature is zero degrees Celsius; a 20% change in relative humidity horizontally would count for a half cycle phase difference in the interferogram. Hanssen *et al.*, (1999) reported that at spatial scales of less than about 50 km, the interferogram phase will track mainly lateral variation of the wet delay e.g. cloud droplets can produce a maximum delay of several millimeters.

2.3 Tropospheric refractive delay

In general, the troposphere can be divided into a wet layer (at about 0–10 km above the surface) and a dry layer (at 10–50 km). For a signal coming from the zenith direction, assuming a spherically symmetric atmosphere, the atmospheric zenith total delay (ZTD) can be given as (Li, 2005):

$$ZTD = \int_{H_0}^{H} [n-1]\, dh = 10^{-6} \int_{H_0}^{H} N dh \qquad (8)$$

Where H_0 is the geocentric height of the site above the geoid, and H is the geocentric height of the troposphere above the geoid. The refractive index is expressed in terms of refractivity N where $N = 10^6 \times (n - 1)$. Where n is the

refractivity index for any medium. In clear air, the typically value is around 1.0003. N, is a function of its temperature, pressure and water vapor pressure. The refractivity can be expressed as (Davis *et al.,* 1985; Li *et al.,* 2005):

$$N = k_1 R_d p + k_2 R_v Z_w^{-1} + k_3 R_v \frac{Z_w^{-1}}{T} \tag{9}$$

Where ρ is the total mass density of the air. R_d and R_v are the specific gas constants for dry air and water vapor, and $k_2 = k_2 - (R_d / R_v)\, k_1 = 17 \pm 10$ [$KhPa^{-1}$]. Z_w is the inverse compressibility factors (corrections for non-ideal-gas behavior) for water vapor; T is the absolute temperature in degree Kelvin. It should be noted that the first term on the right hand side of Equation (15) depends only on surface pressure and not on the wet/dry mixing ratio, which is called the hydrostatic refractivity (N_h), whilst the remaining two terms form the wet refractivity (N_w), which depends solely on water vapor distribution. Thus

$$N = N_h + N_w \tag{10}$$

Using Equations (14) and (15) in Equation (16), the zenith troposphere delay can be expressed as:

$$ZTD = 10^{-6} \int (N_h + N_w)\, dh \tag{11}$$

$$= 10^{-6} \left(k_1 R_d \int p\, dh + \int \left(k_2 \frac{P_w}{T} Z_w^{-1} + k_3 \frac{P_w}{T^2} Z_w^{-1} \right) dh \right) \tag{12}$$

$$= ZHD + ZWD \tag{13}$$

The dry term (hydrostatic) accounts for roughly accounts for 90% of the total delay. However, the hydrostatic delay observed in interferograms is smooth as well and manifests itself usually as a phase trend of maximally a few millimeters over the entire interferogram (Hanssen, 1996). The wet delay is much smaller than the hydrostatic delay, varying roughly from 0 to 30 cm between the poles and the equator and from a few to about 20 cm during the year at mid-latitudes (Elgered, 1993; Li *et al.,* 2005). However, the phase delay due to water vapor gradients becomes dominant since the interferogram is observed in differential mode.

These theoretical studies show that the sensitivity of the tropospheric refractivity is highest for spatial variation in water vapor content, between 4 and 20 times greater than for temperature variation. This sensitivity, in combination with the fact that water vapor exhibits a strong spatial variability, supports the interpretation of small scale (< 50 km) phase delay variations in terms of water vapor (Hanssen, 2001).

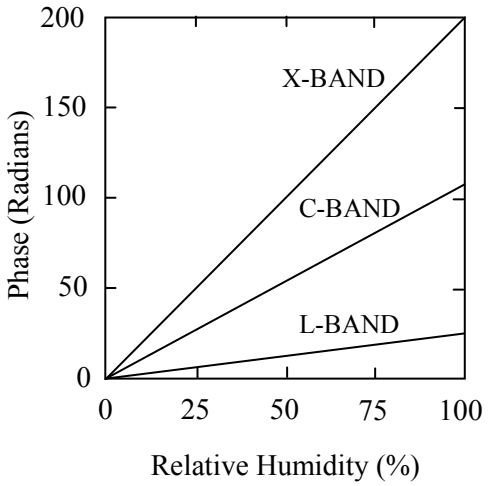

Figure 2.3 Atmospheric phase delay due to the humidity variation at three SIR-C/X-SAR wavelengths. (Adapted from Zebker et al., 1997)

2.4 Mitigations of atmospheric effects

Various methods have been developed for mitigating the atmospheric effects on InSAR measurements and can be classified into two categories based on whether external data is needed (Ding et al., 2008). First category uses external data for the mitigation such as ground meteorological observations, GPS data, satellite water vapor products such as those from MERIS and MODIS. The second category is mainly based on numerical analysis and no external data is needed during the mitigation process, including the pair-wise logic, the stacking, the correlation analysis, and the Persistant Scatterer method. Each of the methods developed has its advantages and disadvantages. However, the most suitable method should be also chosen based on the number of SAR image available. Table 2.1 summarizes mitigation methods based on the use of external data and possible data needed for each method.

Table 2.1 Summarizes atmospheric mitigation methods

Mitigation method	Possible with limited data	Need a lot of data
No external data	Pair-Wise Logic Correlation Analysis	Stacking Persistant Scatterer
With external data	MODIS data MERIS data	Ground meteorological GPS observations

2.4.1 Pair-wise logic

The identification of significant localized atmospheric signal is possible using linear combinations, or *pair-wise logic* (Massonnet and Feigl, 1995). By comparing multiple interferograms of the same scene, several types of potential artifacts can be recognized and discounted. Hanssen (2001) suggested to sum or subtract two interferograms that use a common SAR image for removing atmospheric anomalies. It is effective when the atmospheric anomalies exist only in the common SAR image of the two interferograms. Massonnet and Feigl (1995) apply the technique to the area

around the 1992 Landers, California earthquake using SAR images acquired by the ERS-1 satellite. Two atmospheric signatures were identified and separated using the pair-wise logic. Also, the method was used to find a 25x20 km^2 kidney-shaped feature caused by ionospheric perturbations of the same area.

2.4.2 Correlation analysis

In case of atmospheric correction, the correlation method does not aim to remove atmospheric noise from a SAR interferogram, but instead manage to extract the common (correlated) deformation signals within two SAR interferograms (Fruneau and Sarti, 2000). Crosetto *et al*. (2002) estimated atmospheric component of the interferometruc phase by adopting a filtering and prediction procedure, which exploits the phase over stable areas identified in the vicinity of the analysed subsidence area. Usai (2000) used a correlation analysis with D-InSAR to identify the presence of the deformation signal and determine the spatial homogeneity of features within a set of pixels which comprises all effects other than real deformation e.g. atmospheric effects. Sarti *et al*. (1999) proposed to characterize the atmospheric artifacts in SAR interferograms and to remove them through analyzing the correlation between interferograms. Sarti *et al*. (2000) pointed out the advantages of the correlation analysis method over other methods (e.g. stacking and the persistent scatterer) when the number of available SAR images is not large and also, no external data are needed. The method however, results with weak correlation may lead to insufficient atmospheric effect reduction.

2.4.3 Stacking

Stacking takes advantage of the fact that any geodetic signal is likely to persist through several interferograms, whereas atmospheric noise is more nearly random over timescales longer than a day thus, stacking interferograms tends to enhance the geodetic signal and average out the noise which reduce the errors by $1/\sqrt{N}$, where N is the number of interferograms (Hole *et al*., 2007). Williams *et al*. (1998) and Emardson et al. (2003) suggested stacking and calibration methods can be used simultaneously to reduce the effect of atmospheric distortion in SAR interferometry and increase the signal-to-noise ratio. Main limitation as pointed out by Ferretti *et al*. (2000) found that the method works when there are only linear ground deformations as non-linear deformations can be lost in the process of stacking.

2.4.4 Permanent Scatterers

The Permanent Scatterers (PS) InSAR is a multi-image algorithm for DInSAR analysis aimed at extracting surface deformation measurement on a sparse grid of coherent radar targets. In PSInSAR, the atmospheric effects are modeled as linear phase ramps in the azimuth and the range directions. Parameters of an atmospheric model are estimated jointly with other unknowns such as the DEM errors and the LOS ground deformations at the permanent scatterers (Ferretti *et al.*, 2005). Ferretti *et al.* (2001) reported that PSInSAR improved estimation of local topography and terrain motions over Ancona, Italy and Pomona, California. Hooper *et al.* (2004) modified the PSInSAR algorithms and able to extract the temporal and spatial pattern of deformation even where conventional interferograms showed almost complete decorrelation. A shortcoming also stated, that a significant number of SAR images over the same area, typically over 30, are needed to get reliable results.

2.4.5 MODIS

The near-IR water vapor products provided by the Moderate Resolution Imaging Spectro-radiometer (MODIS) have a spatial resolution of 1 km×1 km (at nadir). The high resolution water vapor products appear to be very useful for modeling and correcting atmospheric effects on InSAR with its high spatial resolution when compare to other methods. Li *et al*. (2003a) first presented some results of using MODIS data to correct atmospheric effects on InSAR over Mount Etna and Los Angeles. MODIS near IR water vapour product was applied to reduce tropospheric effects in ERS-2 SAR images. The time difference between MODIS and ERS-2 passes were 20 minutes and 40 minutes. The differences of LOS path delays (single way) varied from –6.8cm to 4.6cm the values closer to zero imply the MODIS correction was effective.

Li *et al*. (2005) proposed an integration of MODIS and GPS data for InSAR atmospheric correctionover SCIGN region, California, where dense GPS data are mainly used to calibrate the MODIS PWV data. The correction results from one of the two ERS-2 interferograms showed that phase variation of the unwrapped interferogram decreased from 2.66 radians without correction to 1.98 radians after applying the GPS/MODIS integrated water vapor correction model. Similary to the other interferogram, phase variation of the unwrapped interferogram decreased from 2.48 rad before correction to 1.47 radians after correction implying that both of the unwrapped interferograms were much flatter after correction. Also, comparisons between GPS and InSAR range changes in the satellite LOS showed that the RMS difference decreased from 1.0 cm before correction to 0.7 cm after correction, while the second one decreased from 1.1 cm before correction to 0.5 cm after correction which indicating that the GPS/MODIS integrated correction model improved the interferogram significantly.

2.4.6 MERIS

The Medium Resolution Imaging Spectrometer (MERIS) onboard the Envisat satellite allows for global retrieval of PWV every three days therefore can acquire water vapor data simultaneously with the Advanced SAR (ASAR); therefore offer an opportunity for the atmospheric effects on ASAR measurements to be accurately modeled. Li *et al*. (2006a) assessed the potential of using MERIS near-infrared water vapor products to correct ASAR interferometric measurements. A comparison of MERIS and GPS-PWV showed an excellent agreement with a standard deviation of 1.1 mm. It was found that MERIS overestimated PWV against GPS under both very dry (PWV 0.5mm) and very wet (PWV.25mm). However, since the MERIS/GPS scale was around 1.02 with a limited range of PWV values and the RMS difference between MERIS and GPS was1.1 mm, which is well below the estimated accuracy of both techniques, GPS data are not required to calibrate MERIS data, particularly under moderate conditions.

Li *et al*. (2006b) demonstrated the successful application of a MERIS water vapor correction model to ENVISAT ASAR data for the first time in the SCIGN region. Comparisons between GPS and InSAR range changes in the LOS showed that the RMS difference decreased from 0.89 cm before correction to 0.54 cm after correction. Another result over the same test area, it was found that the phase variation decreased from 1.73 radians before correction to 1.22 radians after

correction, and the RMS difference between GPS and InSAR decreased from 0.83 cm to 0.59 cm. All of which indicates that the application of this MERIS correction model improved this interferogram

2.4.7 Ground meteorological

Hanssen (1996) gave a first quantitative evaluation of observed effects in SAR interferograms of the Netherlands using Saastamoinen tropospherical model couple with standard meteorological information. The results showed that atmospheric models were mostly too generalized to explain the artifacts that could occur within one interferogram. The main limitation when using meteorological data to mitigate InSAR atmospheric effects is due to the poor accuracy and the usually very sparse distribution of meteorological stations.

2.4.8 GPS

Bonforte *et al*. (2001) demonstrated congruence between the tropospheric zenith delays estimated from GPS observations and from tropospheric models and meteorological data. Observations from the results of GPS analysis highlight that the compensation methods of SAR interferograms, requiring ground-based meteorological data, might be improved by their calibration based on data from both the GPS network. Webley *et al*. (2002) proposed a procedure to use the water vapor delays derived from the GPS observations to calibrate the atmospheric effects on InSAR. Li *et al*. (2006c) generated the mean atmospheric delay map using 14 GPS stations over Mt. Etna to corrected a SAR interferogram and achieved 27.2% overall improvement in the accuracy of the InSAR measurements. In conclusion, using GPS observations depend primarily in the algorithms used to interpolate the spatially sparse GPS measurements. Therefore, the accuracy of the corrections depends on how much atmospheric delays can be retrieved at the unsampled locations from the sparse GPS measurements.

In conclusion, when limited set of data is the major constraint, the possibility of mitigation goes to the method of Pair-Wise Logic or Correlation Analysis and the use of satellite water vapor products. For the latter, the major problem is that it is very difficult to have simultaneous acquisitions with other SAR images other than ASAR.

2.5 SRTM DEM

Producing a differential interferogram requires two interferograms, the deformation pair and the topographic pair. After all images are aligned in the same grid, the topographic pair needs to be unwrapped and scaled according to the baseline ratio between the two interferograms. Subtracting this unwrapped, scaled topographic pair from the deformation pair yields the differential pair. In the case of the two-pass approach, with known imaging geometry, DEM data is mapped from an orthogonal cartographic or geographic coordinate system to SAR image coordinates, and then an interferogram can be synthesized. The simulated interferogram can be applied to remove the topographic phase, pixel by pixel, to leave only the phase due to deformation if there are no atmospheric and other effects. The two-pass method has the advantage of requiring only two spatially coherent radar images, but it also

requires an accurate DEM from some other source (e.g., SRTM). Typically, a DEM with a cell size of 30–90m is adequate for this purpose (Dzurisin, 2007).

SRTM collected data over most of the world's land surface between 60 degrees north latitude and 54 degrees south latitude (which is about 80% of all the land on the Earth), during its ten days of operation in February 2000. This radar system included two types of antenna panels, C-band and X-band, and the near-global DEMs were made by the Jet Propulsion Laboratory (JPL) from the C-band radar data. The X-band radar data were used to create slightly higher resolution DEMs but without the global coverage. The SRTM data has a spatial resolution of 90 metres and a vertical absolute accuracy of less than 7 metres (Farr and Kobrick, 2000). The horizontal datum is WGS84, and the vertical datum is the WGS84 EGM96 geoid (NIMA, 1997; Bamler, 1999).

2.6 TerraSAR-X

TerraSAR-X is a side-looking X-band synthetic aperture radar (SAR) based on active phased array antenna technology. The active antenna allows not only the conventional stripmap imaging mode but additionally spotlight and ScanSAR mode (Eineder et al., 2006). From data used in this study is acquired with stripmap mode, then only detail description on this specific mode is reviewed.

Table 2.2 Summarizes the characteristic values of the platform and the SAR instrument (Eineder et al., 2006).

Orbit and Attitude Parameters	
Nominal orbit height at the equator	514 km
Orbits / day	$15\ ^{2}/_{11}$
Revisit time (orbit repeat cycle)	11 days
Inclination	97.44°
Ascending node equatorial crossing time	18:00 ± 0.25 h (local time)
Attitude steering	"Total Zero Doppler Steering"

This is the basic SAR imaging mode as known e.g. from ERS-1 and other satellites. The ground swath is illuminated with a continuous sequence of pulses while the antenna beam is pointed to a fixed angle in elevation and azimuth. This results in an image strip with constant image quality in azimuth. In figure 2.4, the stripmap mode geometry is illustrated. The characteristic parameters of this mode are listed in Table 2.3.

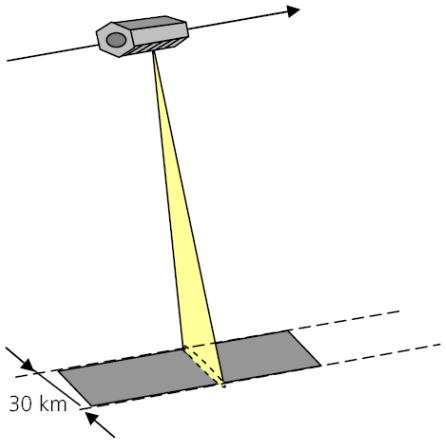

Figure 2.4 Imaging geometry in strip map mode (after Eineder et al., 2006).

Table 2.3 Characteristic parameters of stripmap mode

Parameter	Value
Swath width (ground range)	30 km single pol. 15 km dual pol.
Acquisition length	< 1650 km
Full performance incidence angle range	20° - 45°
Data access incidence angle range	15° - 60°
Number of elevation beams	ca. 27
Azimuth resolution	3 m
Ground range resolution	1.55 m - 3.21 m (@45°.. 20° incidence angle)
Polarizations	HH or VV (single) HH/VV, HH/HV, VV/VH (dual)

2.7 MODIS

2.7.1 Product Description

The MODIS Precipitable Water product consists of column water-vapor amounts. During the daytime, a near-infrared algorithm is applied over clear land areas of the globe and above clouds over both land and ocean (Gao and Kaufman, 2003). Over clear ocean areas, water-vapor estimates are provided over the extended glint area. An infrared algorithm for deriving atmospheric profiles is also applied both day and night for Level 2. There are two MODIS Water Vapor data product files: MOD05_L2, containing data collected from the Terra platform; and MYD05_L2, containing data collected from the Aqua platform.

The Level 2 data are generated at the 1-km spatial resolution of the MODIS instrument using the near-infrared algorithm during the day, and at 5x5 1-km pixel resolution both day and night using the infra-red algorithm when at least nine FOVs are cloud free. The infrared-derived precipitable water vapor is generated as one

component of product MOD07, and simply added to product MOD05 for convenience. The solar retrieval algorithm relies on observations of water-vapor attenuation of reflected solar radiation in the near-infrared MODIS channels so that the product is produced only over areas where there is a reflective surface in the near IR (Gao and Kaufman, 2003).

Table 2.4 Science Data Sets for MODIS precipitable water vapor product (Gao and Kaufman, 2003).

Data Group	Science Data Sets (HDF Layers (43))	Units	Data Type	Fill Value	Valid Range	Scale Factor
1 km	1 km Atmospheric Optical Depth Band 1: (AOT retrieval residual values)	none	16-bit signed integer	60	0 - 5,000	0.001
	1 km Atmospheric Optical Depth Band 3	none	16-bit signed integer	60	0 - 5,000	0.001
	1 km Atmospheric Optical Depth Band 8: (Angstrom exponent values)	none	16-bit signed integer	60	0 - 5,000	0.001
	1 km Atmospheric Optical Depth Model	none	8-bit unsigned integer	0	1 - 5	1
	1 km water vapor	g/cm^2	16-bit unsigned integer	0	0 - 5,000	0.01
	1 km Atmospheric Optical Depth Band QA	Bit Field	16-bit unsigned integer	0	0 - 65,535	1
	1 km Atmospheric Optical Depth Band CM	none	8-bit unsigned integer	0	0 - 19	1
	250 m Surface Reflectance Band 1	Reflectance	16-bit signed integer	-28,672	-100 - 16,000	0.0001

2.7.2 Instrument Characteristics

MODIS is a major facility instrument on the EOS polar orbiting satellite platforms (Asrar and Greenstone, 1995; King et al., 1992; Salomonson et al., 1989; Gao and Kaufman, 2003) designed to measure biological and physical processes on a global scale every 1 to 2 days. It is a 36-channel scanning radiometer covering the spectral region 0.4 - 15 mm.

Five near-IR MODIS channels are useful for remote sensing of water vapor. The positions and widths of these channels are given in table 2.5 and illustrated in figure 2.5. Two atmospheric water vapor transmittance spectra for the Tropical and Sub-Arctic Winter Models in LOWTRAN7 with a solar zenith angle of 45 degrees and a nadir-looking geometry are also shown in figure 2.5. The channels at 0.865 and 1.24 mm are non-absorption channels present on MODIS for remote sensing of

vegetation and clouds. The channels at 0.935, 0.940, and 0.905 mm are water vapor absorption channels with decreasing absorption coefficients. The strong absorption channel at 0.935 mm is most useful for dry conditions, while the weak absorption channel at 0.905 mm is most useful for very humid conditions, or low solar elevation.

Table 2.5 Positions and widths of five MODIS near-IR channels used in water vapor retrievals (Gao and Kaufman, 2003).

MODIS Channel #	Position (μm)	Width (μm)
2	0.865	0.040
5	1.240	0.020
17	0.905	0.030
18	0.936	0.010
19	0.940	0.050

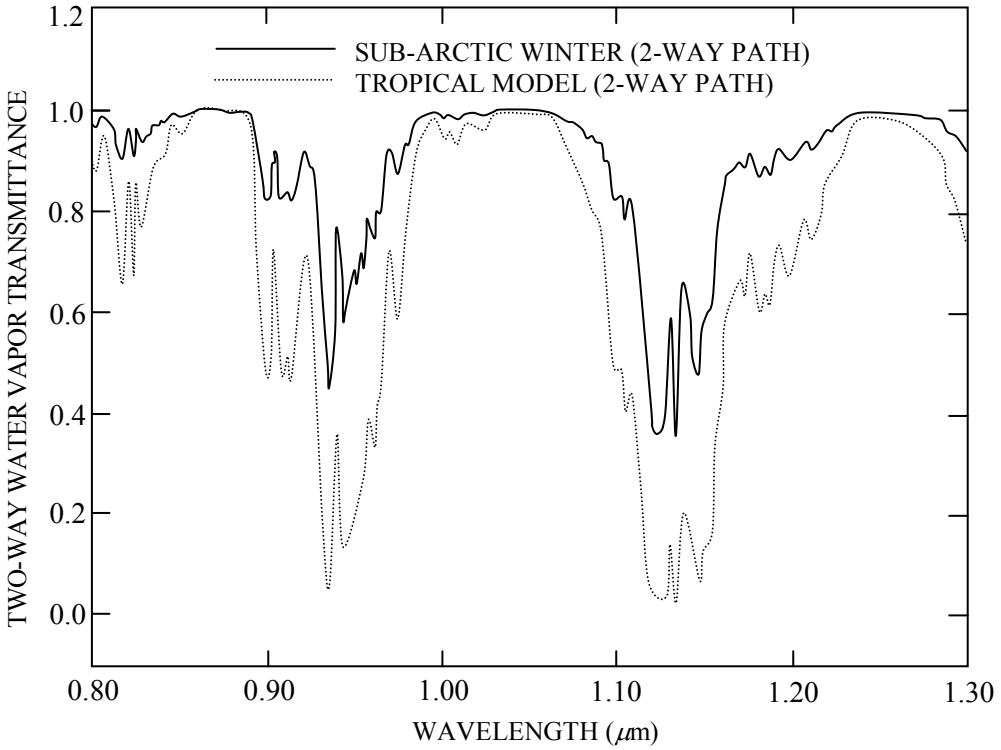

Figure 2.5 Positions and widths of five MODIS near-IR channels marked in thick horizontal bars, and 2-way atmospheric water vapor transmittance spectra for Tropical and Sub-Arctic Winter Models in LOWTRAN7 (Kneizys *et al*., 1988; Gao and Kaufman, 2003) with a solar zenith angle of 45 degrees and a nadir-looking geometry.

2.8 D-InSAR Processing

This step has been performed using the SARScape 4.0 software, a commercial SAR interferometry module running on ENVI 4.5. This module supports the processing of Interferometric SAR (2-pass interferometry, InSAR) and Differential Interferometric SAR (n-pass interferometry, DInSAR) data for the generation of Digital Elevation Model, Coherence, and Land Displacement maps. SAR data which includes information of coordinates; phase and amplitude are imported in SARScape

software using *Import* function. The selected raw data are then processed to convert SAR signals to image products like Single Look Complex (SLC) using *Focusing* function. A ω-k frequency domain algorithm has been implemented to guarantee the lowest phase distortion and to preserve the original interferometric coherence. Noted that the final products used for the tests are mainly the coherence and phase images in which both the multi-looking window and the coherence estimation window are of 2 x 10 pixels. The overall interferometric processing includes the following steps (CREASO, 2007):

2.8.1 Interferogram generation

First of all, *Coarse and Fine Coregistration* provides the proper parameters in order to align the same points in the two images. Then, *Common Doppler Bandwidth Filtering* is applied if there is a difference in the Doppler Centroids, this step allows minimization of the decorrelation. After that, *Spectral shift filtering* is performed on the image pair. The next step is optional, *Coarse DEM flattening*, which synthetic fringes are generated from a coarser resolution DEM or ellipsoidal height, using a backward geocoding approach, and then cross-multiplied by the SAR interferogram. This step allows removal of most of the low frequency components of the wrapped phase, to ease the following phase unwrapping. Finally, the flattened complex interferogram is filtered using optional function called *Adaptive Filtering*, to improve the phase signal to noise ratio (SNR).

2.8.2 Phase unwrapping

The filtered interferogram is *Phase Unwrapped* by using a region growing approach. Optional *Phase edit* can be used to correct some unwrapping errors in a semi-automatic or completely manual way. Geometry optimization based on Ground Control Points (GCPs) or *Baseline Fit*, the orbits are refined in order to obtain an accurate conversion of the phase information to height and a proper geo-location. Both manual and automatic procedures for the identification of the most suitable image pixels to be used as GCPs are implemented. The synthetic phase is added back to the unwrapped phase, so that the final DEM is derived only from the SAR data.

2.8.3 Phase to displacement

The phase values are converted to displacement and geo-coded onto a map projection. The user can enter a specific direction (azimuth angle) and inclination angle along which he assumes that the main deformation occurred, or even enter a-priori known deformation field as input. For the generation of displacement maps it is mandatory to run a second iteration of the processing, from the interferogram flattening to the phase unwrapping, after the execution of the baseline fit step (which is aimed at correcting orbital inaccuracies).

2.9 Inverse Distance Weighted Interpolation

One of the most commonly used techniques for interpolation of scatter points is inverse distance weighted (IDW) interpolation. From the study by Janssen *et al*. (2004) who tested the effectiveness of three algorithms in interpolating the GPS derived atmospheric delays and found that the inverse distance weighting and Kriging interpolators are better than the spline interpolator. Inverse distance weighted methods

are based on the assumption that the interpolating surface should be influenced most by the nearby points and less by the more distant points. The interpolating surface is a weighted average of the scatter points and the weight assigned to each scatter point diminishes as the distance from the interpolation point to the scatter point increases.The simplest form of inverse distance weighted interpolation is sometimes called "Shepard's method" (Shepard 1968). The equation used is as follows:

$$F(x,y) = \sum_{i=1}^{n} w_i f_i \tag{14}$$

Where n is the number of scatter points in the set, f_i are the prescribed function values at the scatter points (e.g. the data set values), and w_i are the weight functions assigned to each scatter point. The classical form of the weight function is:

$$w_i = \frac{h_i^{-p}}{\sum_{j=1}^{n} h_j^{-p}} \tag{15}$$

Where p is an arbitrary positive real number called the power parameter (typically, p=2) and h_i is the distance from the scatter point to the interpolation point or

$$h_i = \sqrt{(x - x_i)^2 + (y - y_i)^2} \tag{16}$$

Where (x,y) are the coordinates of the interpolation point and (x_i,y_i) are the coordinates of each scatter point. The weight function varies from a value of unity at the scatter point to a value approaching zero as the distance from the scatter point increases. The weight functions are normalized so that the weights sum to unity. The effect of the weight function is that the surface interpolates each scatter point and is influenced most strongly between scatter points by the points closest to the point being interpolated.

2.10 Bicubic polynomial interpolation

MODIS bands systematically have a specific relative delay that causes a slight spatial misregistration of corresponding pixels. MODIS is a cross-track scanning mirror system with blocks of 10 sensors for water vapors channels and the double-sided scan mirror sweeps out a swath of the Earth 10 km wide at nadir in each scan (Nishihama *et al.*, 1997; Li *et al.,* 2009). Examination of hundreds of Terra MODIS images revealed that stripes have appeared consistently every 10 lines from the second line in MODIS near-IR images since 2002 and when such a MODIS image is used for atmospheric correction, the impact of the stripes is evident (Gao and Kaufman, 2003). In Li *et al.,* (2009), the erroneous values were replaced with interpolated values using the two neighboring pixels in the along-track direction, however, with the variation in water vapor which was clearly much higher in this

tropical zone than dessert area as in Li's test site in California, better interpolation method should be considered.

From many types of curve-fitting functions, polynomial is widely used because of its unique characteristics. In this experiment, Bicubic polynomial was used as an interpolation method. It is basically to form 10 equations which are the relationships between height value (z) and horizontal parameters (coordinate x,y) in order to solve 10 unknown coefficient values. In this study, we formed 16 polynomial equations for height estimation by the process of least square. General form of bicubic polynomial is shown in equation (17). Suppose the function values f and the derivation f_x, f_y and f_{xy} are known at the four corners (0, 0), (1, 0), (0, 1) and (1, 1) of the unit square. The interpolated surface can then be written

$$p(x,y) = \sum_{i=0}^{3}\sum_{j=0}^{3} a_{ij} x^i y^j \qquad (17)$$

The interpolation problem consists of determining 16 coefficients a_{ij} Matching $p(x,y)$ with the function values yields four equation.

CHAPTER III

METHODOLOGY

3.1 Test area

South-eastern part of Bangkok metropolitan was selected as test area (figure 3.1). An advantage of this test site is that most of the area are urbanized which means a large portion of stable pixels in SAR images remains coherent over time and thus the phase measurement described in eq.1 is valid. Situated far from active faults, tectonic deformation could be assumed to be negligible. The main cause of surface deformation is known to be from land subsidence due to over extraction of groundwater (Phienwej *et al*., 2006). However, the annual rates are known and so can be estimated over the period of repeat SAR acquisitions. Further, the study area is flat with ground elevation gradually decreases from few meters above mean sea level in the north to zero at the coastline. The SRTM DEM that was used to remove topographic phase correspond well with the terrain, which means and the absolute vertical error is much less than +/- 16 m as stated in its design accuracy (Rabus *et al*., 2003) and topographic phase terms can be accurately estimated.

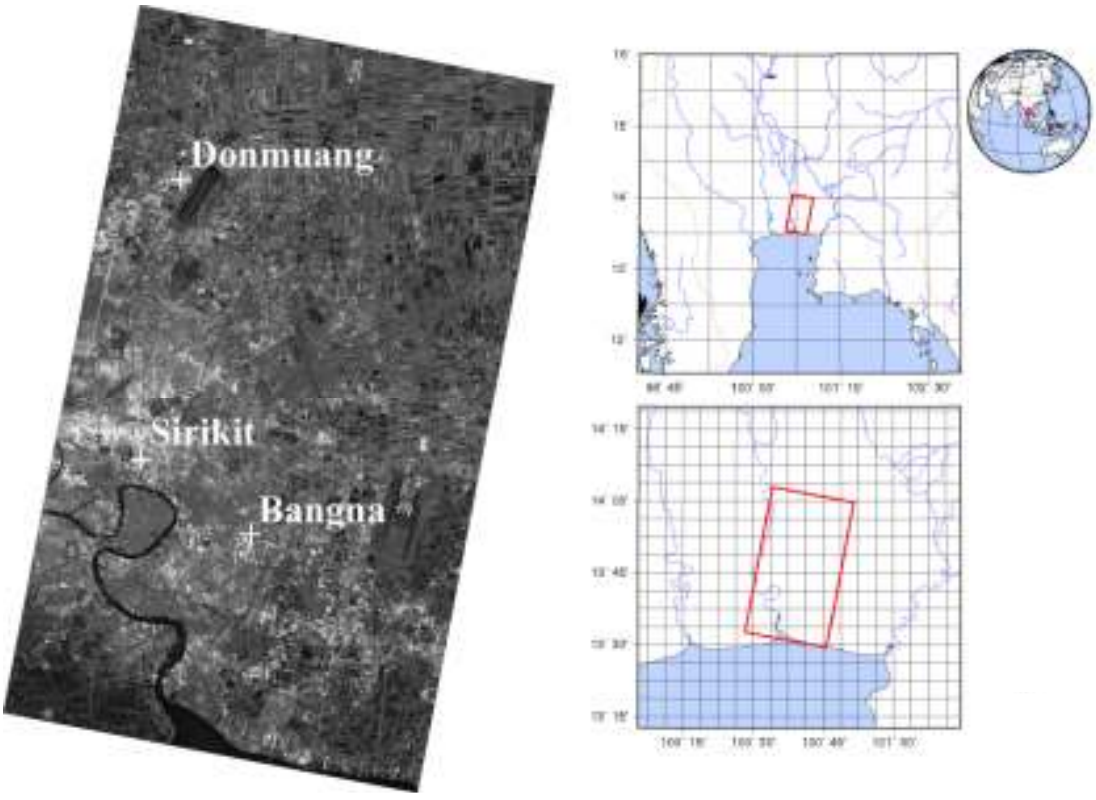

Figure 3.1 TerraSAR-X image track 075 (Descending) acquired on October 30, 2009 over south-eastern Bangkok (http://www.infoterra.de/terrasar-x-archive). Three meteorological stations used in this study are shown; Bangna, Donmuang and Sirikit.

3.2 TerraSAR-X data

Four SAR images were selected from an archive of 23 TerraSAR-X strip-map mode SLC images (descending path, track 075) that had been acquired since September 2009 until June 2010 for the study of Bangkok subsidence. The acquisition in strip-map mode provides SLC images with 3m resolution and a spatial coverage of 30 km x 50 km. The location of study area and the coverage of TerraSAR-X image are shown in figure 3.1. As the study aims to correct atmospheric effect in the interferogram, the main selection criterion is that cloud-free MODIS-PWV data on the same date of SAR acquisition is available. The criterion can rarely be satisfied in tropical South East Asia where the number of completely cloud-free is very low, thus the four images were chosen on the date that had least cloud-covered MODIS-PWV data.

Six interfergrams could be formed by pairing any two of the four chosen TerraSAR-X SLCs. As coherence decreases over time, temporal separation should be kept to minimum in the selection of SLC pairs. Further, the magnitude of deformation phases in the interferogram formed from pairs with small temporal baseline became small. Over the same area, the maximum subsidence rate during 2005-2009 periods determined from a combined persistent scatterer/small baseline InSAR technique was at maximum of 15 mm/yr (Aobpaet *et al.*, 2010). With this rate, monthly subsidence was less than 1.3 mm and ϕ_{def} was definitely less than 15^{o}, significantly less than system noise of 35^{o} as reported in (Poncos *et al.*, 2008). The deformation phase term could then be neglected in the interferogram with less than 1 month temporal baseline. As a result, 2 SLC pairs, with the maximum of 22-day separation (2 revisit periods), were chosen for the processing to form 2 interferograms for further study. Details of both SLC pairs were shown in table 3.1.

Table 3.1 Basic statistics of the 2 interferograms

Int.	Track	Date 1	Date 2	days	$B_{\perp}$ (m)	B_c (m)	H_A (m)	S (radian)
1	075	30 Oct 09	21 Nov 09	22	42.4	3,970	213.2	0.47
2	075	2 Dec 09	24 Dec 09	22	9.1	3,970	995.1	0.10

$B_{\perp}$ = Perpendicular baseline (m)
B_c = Critical baseline (m)
H_A = Height ambiguity (m)
S = Phase error due to 16m topographic uncertainty of SRTM DEM
Note: TerraSAR acquisition time is 23:15 UTC or 6:15 local time/ MODIS acquisition time is 3:30 UTC or 10:30 local time

3.3 Interferogram formation

The processing was done in SARScape 4.0 which is a special extension running on ENVI 4.5. The usual steps for 2-pass DInSAR are image co-registration, interferogram formation, interferogram flattening and removal of the topographic phase term by the use of DEM. Special attention was given to the removal of topographic contributions from interferograms. An SRTM DEM with a spatial resolution of 90 m was used for this purpose. SRTM DEM is canopy based (Li, 2005), which means it represents a height related to the average phase centre of the radar echoes from scattering elements in the resolution cell such as trees or buildings, not to the ground. While this characteristic may cause problems for other applications required ground surface height, it was advantageous in this case. With large height ambiguity, the 16 m vertical error of the SRTM DEM results into 26.9^{o} and 5.7^{o} in inteferogram 1 and 2 respectively. These phase from DEM error were below the phase noise level of 35^{o} of TerraSAR-X images (Poncos *et al.*, 2008) and so negligible. After removing topographic phase, interferograms were multilooked (2 in rage and 10 in azimuth direction), filtered (5x5 moving average windows), unwrapped, and geocoded to UTM map plane.

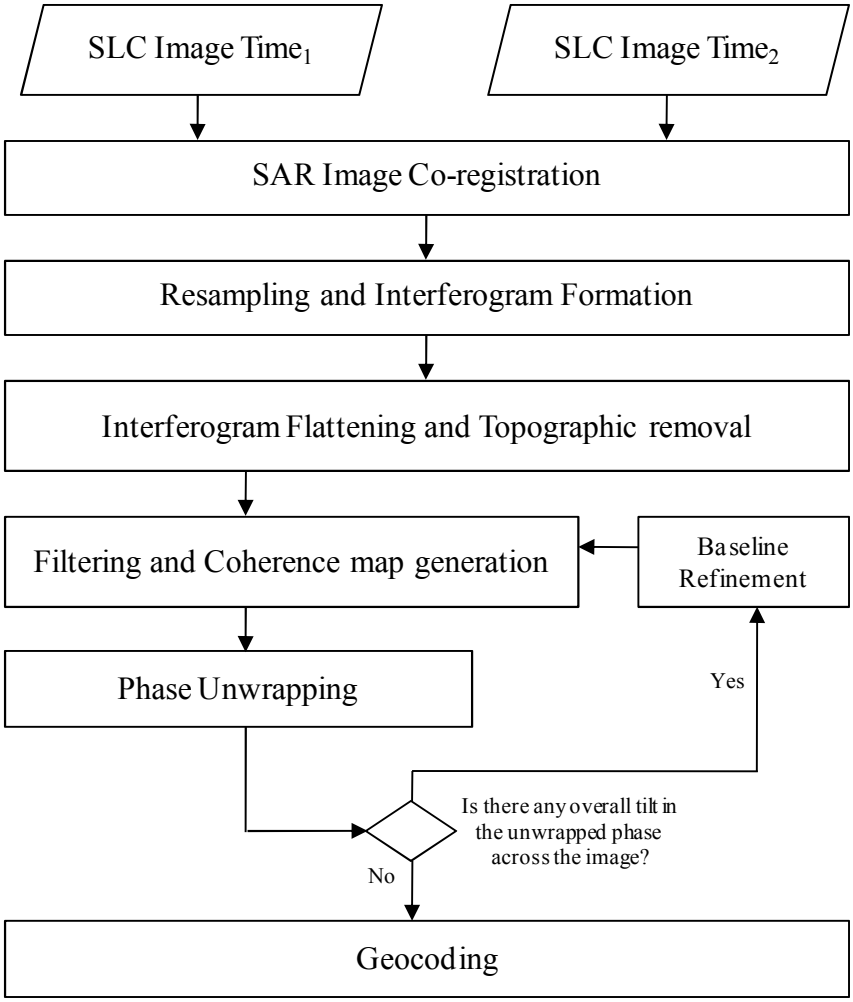

Figure 3.2 General interferometric processing steps in SARScape 4.0 (CREASO, 2007)

3.4 Atmospheric phase term

In this thesis, an attempt to reduce water vapor effects was made, focusing on the use of independent datasets including MODIS-PWV data and ground-based meteorological observations. The Saastamoinen model had been used for tropospheric delay computation in this study using meteorological parameters; relative humidity (RH) and temperature (T), based on the assumption of the linear decrease in temperature with height and the relationship between total pressure and water vapor partial pressure to compute the zenith wet delay (Saastamoinen, 1972). The atmospheric phase term in this study was computed by 3 different methods, the main processing steps of each were shown in figure 3.3. The first method (referred to hereafter as method 1) was to use MODIS-PWV directly to compute the atmospheric phase as in Saastamoinen model. The second method was to employ meteorological data to calibrate MODIS-PWV before phase computation while in the third method, an attempt to further improve the second method by estimating the expected MODIS value at the time of the SAR image acquisitions was made. Processing details on each method were as follow.

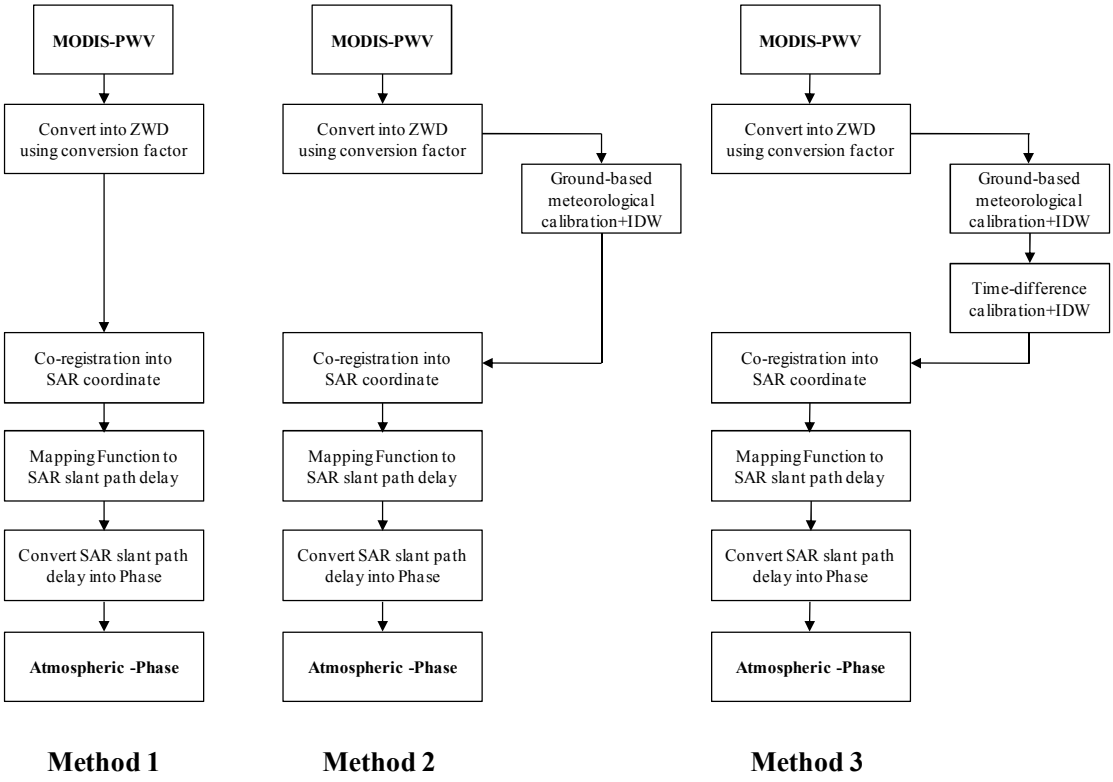

Figure 3.3 Processing flow charts of how to convert the MODIS-PWV data into phase in 3 different methods.

3.4.1 Method 1

MODIS-PWV data with the least cloud-covered were selected since there was no completely cloud-free data within the test area during the TerraSAR-X acquisitions. Satellites scan line errors which values were significantly different in variance and mean of adjacent lines were masked out while the bi-cubic polynomial interpolation method was used to fill in the missing values. Then, PWV data was converted into ZWD using conversion factor using the following relationship:

$$ZWD = \prod \times PWV \tag{18}$$

where Π is a conversion factor which is dimensionless and usually ranges from 6.0 to 6.5. An average conversion factor of 6.2 was adopted in this research (Bevis et al., 1992). It should be noted that since MODIS is a passive tool (one-way acquisition mode) while SAR instrument is the active tool (two-way acquisition mode), the ZWD data were calculated with double value. In order to align MODIS data with the SAR image for the pixel-by-pixel phase correction, the image-to-image co-registration was performed based on the external DEM, in this case using the SRTM DEM as a reference. After that by using the simplest mapping function 1/sin *E* when *E* is the elevation angle, zenith wet delays are converted into slant path delays. With the varying range of TerraSAR-X elevation angle between far range (65 ^{o}) and near range (62 ^{o}). Finally, MODIS water vapor data in slant path delay was divided by TerraSAR-X band wavelength (31 mm) to convert into phase.

3.4.2 Method 2

As reported by Gao and Kaufman (2003), uncertainties in the surface spectral reflectance, sensor calibration, haze, undetected clouds were estimated to be 5-10% and could be up to 14% under hazy conditions. In method 2, it was to employ meteorological data to calibrate MODIS-PWV before phase computation. Following the processing step in method 1 after applied the conversion factor, at this point before the image co-registration, the second method diverted from the usual processing sequence with the insertion of a calibration process. Following the calibration approach made by Li *et al.* (2005) where the GPS data were used to calibrate the MODIS data. As reported by Qu *et al.* (2008) that the zenith delays calculated using ground meteorological data were also in accordance with the GPS observations. In this research, ground-based meteorological data were used for calibration purpose. The Saastamoinen model had been used for zenith wet delay computation in this study since it was a good and accurate method to compute zenith wet delay if surface meteorological data were available (Katsougiannopoulos *et al.*, 2006) and in general better than the others (Kos, 2008) with an estimated accuracy of 3 cm in zenith (Mendes, 1999). Based on the assumption of the linear decrease in temperature with height and the relationship between total pressure and water vapor partial pressure, ZWD can be computed using the following equation (Saastamoinen, 1972):

$$ZWD = 0.002277\left(\frac{1255}{T} + 0.05\right)e_0 \tag{19}$$

Where T is surface temperature in degrees Kelvin.e_0 is surface water vapor partial pressure in hPa and can be derived from the relative humidity RH[%] using:

$$e_0 = \frac{RH}{100e^{(-37.2465+0.213166T-0.000256908T^2)}} \quad (20)$$

As such, the meteorological data covering the scanning time of MODIS acquisition were then selected and compared with MODIS-ZWD data under clear sky conditions during a 2 year-period ranging from December 2008 to February 2010, assuming the relationship between ZWD to be linear:

$$ZWD_{SAAS} = a \times ZWD_{MODIS} + b \quad (21)$$

Where ZWD_{SAAS} is the zenith wet delay computed from the Saastamoinen model at the time of MODIS acquisition while the ZWD_{MODIS} is zenith wet delay computed from MODIS water vapor data. After that, a scale factor (a) computed from each station was spatially interpolated with Inverse Distance Weighting (IDW) method before applied to MODIS data. It should be noted that only ZWD_{MODIS} values within 2σ were brought into comparisons, to which errors could come from some cloudy pixels which are falsely identified as cloud free.

3.4.3 Method 3

Since there was only time intervals of up to 60 minutes between MODIS and ERS data used in Li's experiment, while it is much wider of time interval up to 5 hours difference with the TerraSAR-X data. As reported by Emardson *et al*. (2003), that water vapor values were temporally uncorrelated when their temporal interval was greater than 1 day. Such that, the water vapor condition could differ significantly. In method 3, there was an attempt to improve method 2 by estimating the expected MODIS value (acquired around 11 a.m. local time) at the time of the SAR image acquisition (around 6 a.m.). Following the calibration approach of method 2 but this time, the meteorological data covering the scanning time of MODIS measurement were compared with the meteorological data covering the scanning time of TerraSAR-X during the same 2 year-period, assuming the relationship between ZWD to be linear.

3.5 Integration of MODIS water vapor

Li *et al.* (2005) proposed an integration of MODIS water vapors products for InSAR atmospheric correction. After the interferogram formation, and removal of the topographic signal by use of a DEM, at this point, the step diverts from the usual interferometric processing sequence with the insertion of a MODIS-ZWD data (Li *et al.*, 2005) which was now converted into phase (of the three methods as discussed earlier) and were processed and unwrapped, geocoded and projected into UTM system. D-InSAR processing flowchart with the integration of MODIS water vapor product was shown in figure 3.4.

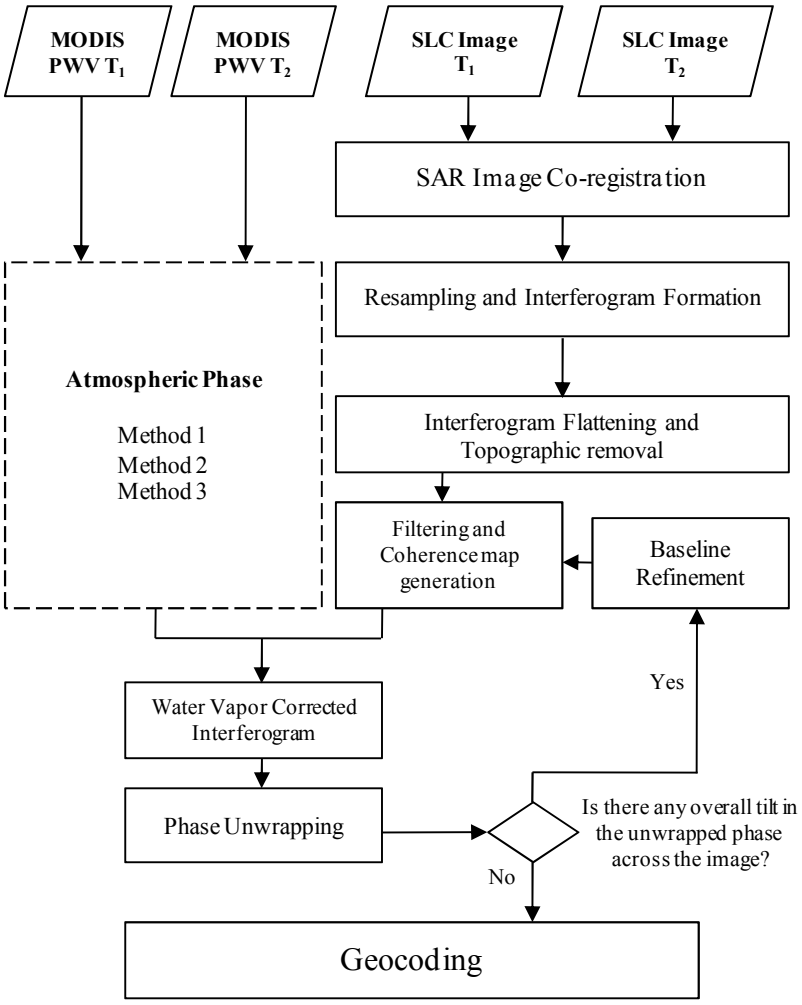

Figure 3.4 DInSAR processing flowchart with the integration of MODIS water vapor.

CHAPTER IV

RESULTS AND DISCUSSIONS

4.1 The Calibration results

The calibration result using ground-based meteorological data indicated that ZWD_{MODIS} was almost identical with ZWD_{SAAS} at Bangna station by an indifferent scale factor of 1.007, while at Donmuang station; it indicated that ZWD_{MODIS} was larger by a scale factor of 1.208. In contrast with Sirikit station, it was found to be smaller than ZWD_{SAAS} by a scale factor of 0.916. The number of valid samples was 49, 50 and 33 respectively, for roughly 25% of all MODIS PWV observations appeared to be cloud free on each meteorological station. Regression results of the ground-based calibration were shown in the left column of figure 4.1. The calibration for the time-difference between ZWD_{MODIS} and $ZWD_{TerraSAR}$ at Bangna, Donmuang and Sirikit meteorological station indicated that $ZWD_{TerraSAR}$ was smaller than that of ZWD_{MODIS} with the scale factor of 0.923, 0.886 and 0.924 respectively. In term of the calibration results, it shows that there were good linear relationships between ZWD_{MODIS} and the ZWD_{SAAS} and also ZWD_{MODIS} with the $ZWD_{TerraSAR}$. Regression results of the time-difference calibration were shown in the right column of figure 4.1.

Finally, the calibration map from scattering meteorological stations was created using the Inverse Distance Weighting (IDW) interpolation. The ground-based calibration map was interpolated from 3 meteorological station points located within the TerraSAR scene, the result was shown in figure 4.2 (left) while the result of the time-based calibration map interpolated with the same station points was shown in figure 4.2 (right).

Table 4.1 Statistics results of MODIS water vapor in all 3 cases

No.	MODIS water vapor-1 (30 Oct-21 Nov 09)	Statistics Results (mm)			
		min	max	mean	std
1	Non-calibrated	-17.1	70.9	21.1	22.9
2	Ground-based calibrated	-17.9	74.0	22.1	23.9
3	Time-based calibrated	-15.2	70.1	20.4	22.3
No.	MODIS water vapor-2 (2 Dec-24 Dec 09)	Statistics Results (mm)			
		min	max	mean	std
1	Non-calibrated	-70.7	27.3	-5.9	12.7
2	Ground-based calibrated	-73.8	28.5	-6.1	13.2
3	Time-based calibrated	-70.4	25.6	-5.8	12.5

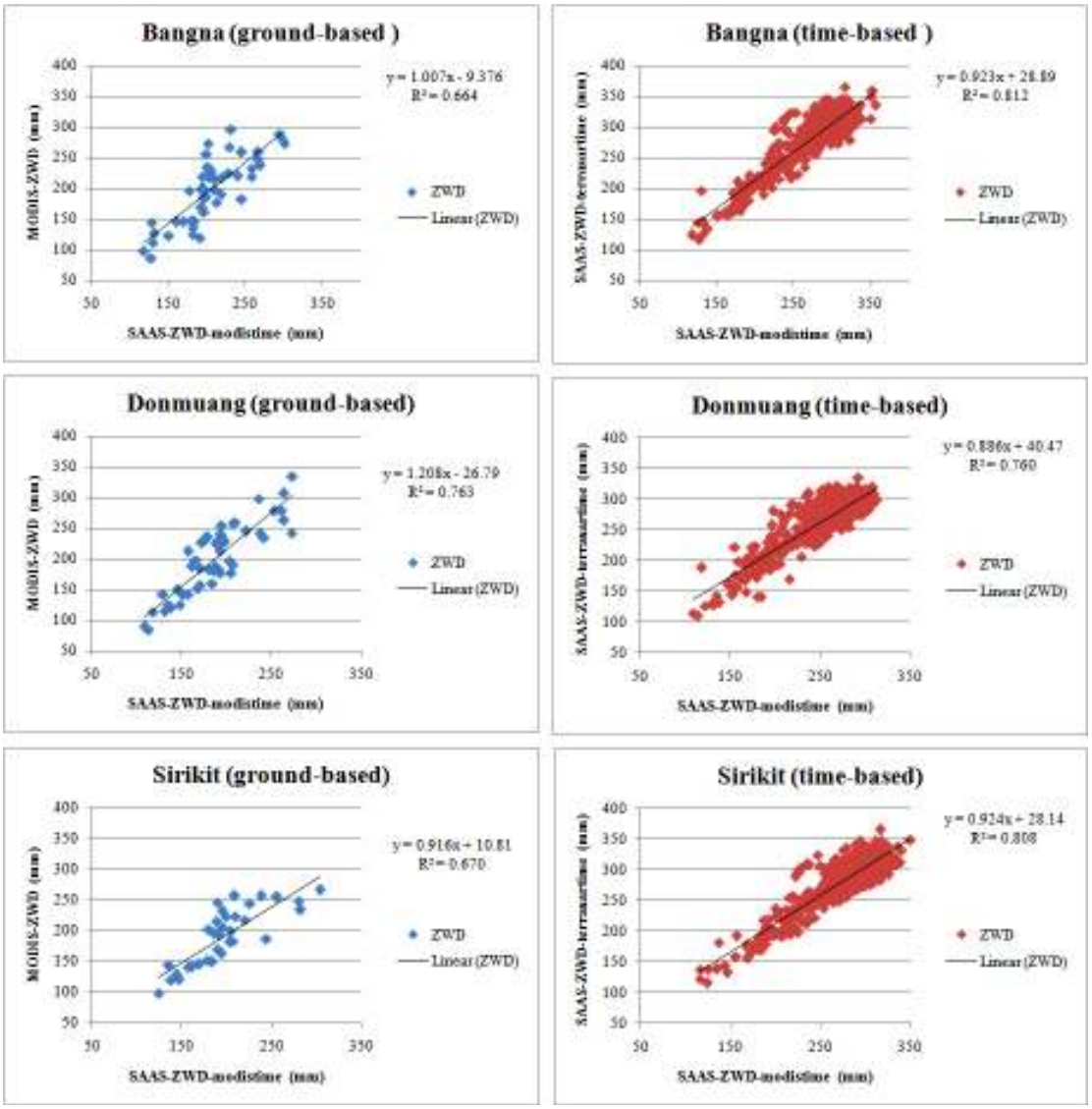

Figure 4.1 Regression results of 3 meteorological stations namely; Bangna, Donmuang and Sirikit.

Table 4.2 ZWD computed from Saastamoinen model at a time of TerraSAR and MODIS acquisitions

Date	ZWD from Saastamoinen model acquisition time every 3 hours						
	4:00	*TerraSAR*[a]	7:00	10:00	*MODIS*[b]	13:00	Shift[c] (mm)
30 Oct 09	265.9	*265.9*	265.8	251.7	*251.2*	233.3	+14.7
21 Nov 09	204.6	*204.4*	184.2	180.5	*180.7*	188.6	+23.7
2 Dec 09	206.8	*206.7*	199.4	199.7	*199.4*	190.9	+7.3
24 Dec 09	230.5	*230.5*	227.5	216.5	*216.0*	203.0	+14.5

[a] TerraSAR time acquisition (23:15 UTC/ 6:15 local time)
[b] MODIS time acquisition (3:30 UTC/ 10:30 local time)
[c] Different ZWD between TerraSAR and MODIS, positive sign (+) implies that ZWD on TerraSAR time was higher
Note: all ZWD are average values computed from 3 stations

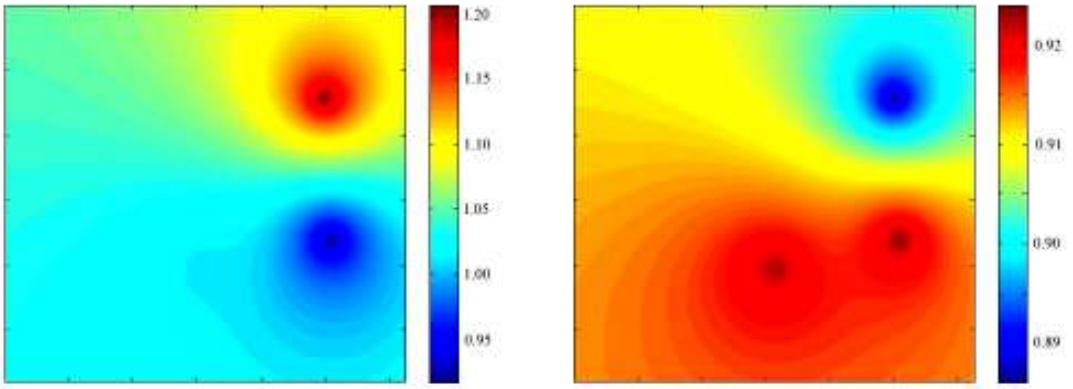

Figure 4.2 The calibration maps which were interpolated using the IDW algorithm from 3 meteorological stations; (left) ground-based, (right) time-based.

4.2 MODIS data

4.2.1 Cloud mask

As MODIS near-IR water vapor retrieval algorithms rely on observations of water vapor absorption of near-IR solar radiation reflected by land, water surfaces and clouds, they are sensitive to the presence of clouds (Li *et al.,* 2009). The MODIS Cloud Mask product is a Level 2 product generated at 1-km and 250-m (at nadir) spatial resolutions. Two cloud mask used for each interferogram were shown in figure 4.3a and 4.3b. It can be seen that there was only 70% on each cloud mask that was cloud free. The average percentages of cloud free area on the month of December during 2006 -2009 within the TerraSAR-X scenes were 70.29, 66.02, 66.16 and 72.48 respectively. Spatial frequency of cloud free conditions from a total of 64 available MODIS water vapor field data on the month of December during 2006 -2009 were shown in figure 4.4. The results corresponded with the study by Li *et al.,* (2009) who investigated the frequency of cloud-free conditions on a global scale using 6 years of Terra MODIS Atmosphere Monthly Global Product (MOD08_M3) from March 2000 to February 2006 and found that the frequencies varied from place to place and from season to season but during winter in South-East Asia region including Thailand, the average cloud-free condition was around 60% – 80% while in other seasons was found to be less than 20%.

4.2.2 Water vapor data

MODIS images have very high geometric quality except one systematic error called BOW-TIE effect caused by multi detector scan line system that could be removed. However, another error caused by multi detector scan line imaging system of MODIS is intense striping (Gao and Kaufman, 2003). MODIS bands systematically have a specific relative delay that causes a slight spatial misregistration of corresponding pixels. MODIS is a cross-track scanning mirror system with blocks of 10 sensors for water vapors channels and the double-sided scan mirror sweeps out a swath of the Earth 10 km wide at nadir in each scan (Nishihama *et al.*, 1997; Li *et al.,* 2009). Examination of hundreds of Terra MODIS images revealed that stripes have appeared consistently every 10 lines from the second line in MODIS near-IR images

since 2002 and when such a MODIS image is used for atmospheric correction, the impact of the stripes is evident (Gao and Kaufman, 2003).

In Li *et al.,* (2009), the erroneous values were replaced with interpolated values using the two neighboring pixels in the along-track direction, however in this study, the Bicubic Polynomial Interpolation method was used instead for it should correspond better with the variation in water vapor which was clearly much higher in this tropical zone than dessert area as in Li's test site in California. Table 4.1 showed the basic statistics of MODIS water vapor fields and the results after the scan line correction using the Bicubic Polynomial Interpolation method. The statistics suggested all the lower values after the correction except the standard deviation of the second water vapor field on Nov 21, 2009 which gave higher value after the correction. The results also showed that the scan line errors in most of the MODIS water vapor fields before correction were over estimated since all the maximum values were masked out and filled in with the interpolated values while only the fourth data on Dec 24, 2009 was under estimated and corrected. Figure 4.5 showed MODIS-PWV data before and after scan line correction.

As MODIS-PWV has different spatial resolutions from SAR data (e.g. 1000 m for MODIS to 25 m of TerraSAR-X), such that, the MODIS-PWV data was re-sampled using Bicubic Polynomial Interpolation method to a grid of 25 m. PWV data was then converted into ZWD using conversion factor. To properly apply water vapor data on SAR interferograms, the step of mapping MODIS-ZWD from the geographic coordinate system to the radar coordinate system (range and azimuth) was needed. In this study, using information from a SRTM DEM and the satellite orbit, a radar image (in the SAR range–azimuth coordinates) could be simulated. With the simulation mapping table and affine transformation parameters, the MODIS-ZWD could be mapped from the geographic coordinate system to the SAR coordinate system.

After using the simplest mapping function 1/sin E when E is the elevation angle as described earlier in section 3.5.1, zenith wet delays were converted into slant path delays as shown in figure 4.6 (top left). It should be noted that MODIS-ZWD data were calculated with double value and all the calibrated parameters from the meteorological data were applied before using the mapping function. Finally, MODIS water vapor data in slant path delay were divided by TerraSAR-X band wavelength (31 mm) to convert into phase as shown in figure 4.6.

Table 4.3 Basic statistics before and after the scan line correction.

Int.	Date	Before correction (mm)				After correction (mm)			
		Min	Max	Mean	Std	Min	Max	Mean	Std
1	30 Oct 09	55.5	387.8	243.4	12.3	55.5	269.3	239.9	12.1
	21 Nov 09	111.5	241.9	201.0	3.7	111.5	225.3	199.4	5.2
2	2 Dec 09	95.6	464.9	203.5	8.0	95.6	242.6	196.1	7.3
	24 Dec 09	130.7	377.0	221.6	3.3	130.1	235.5	217.0	3.7

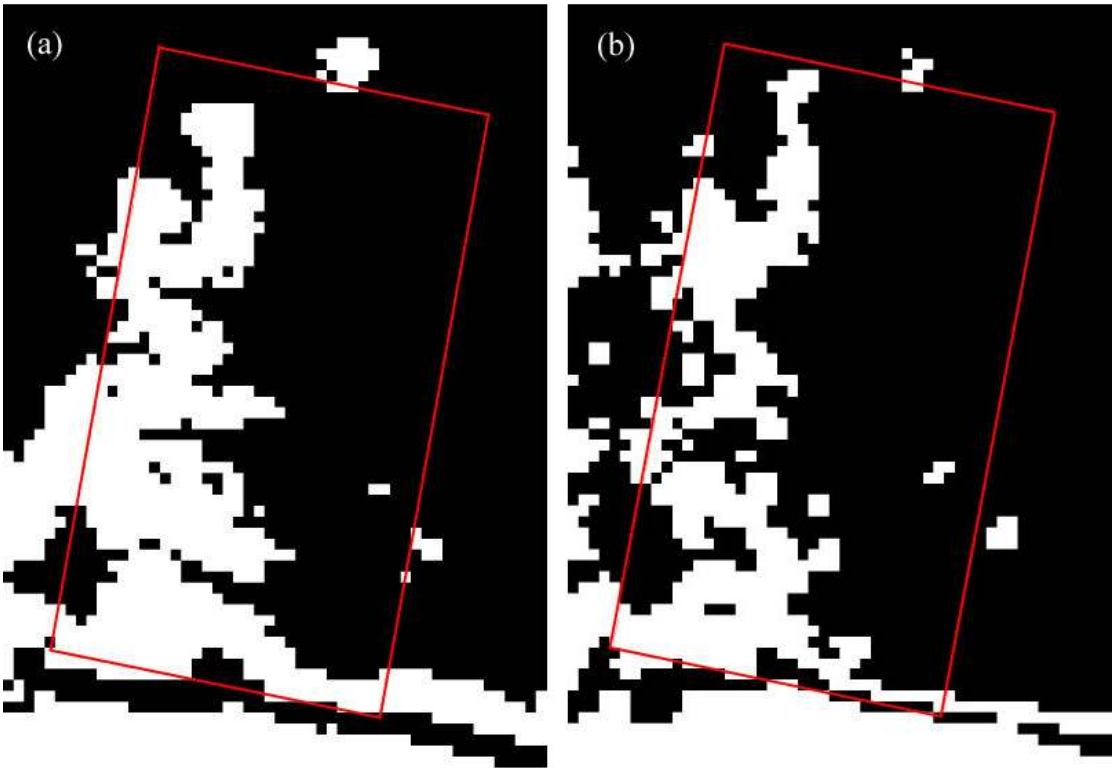

Figure 4.3 (a) cloud mask map of interferogram-1 (white color represents cloudy area, black as cloud free area), (b) cloud mask map of interferogram-2.

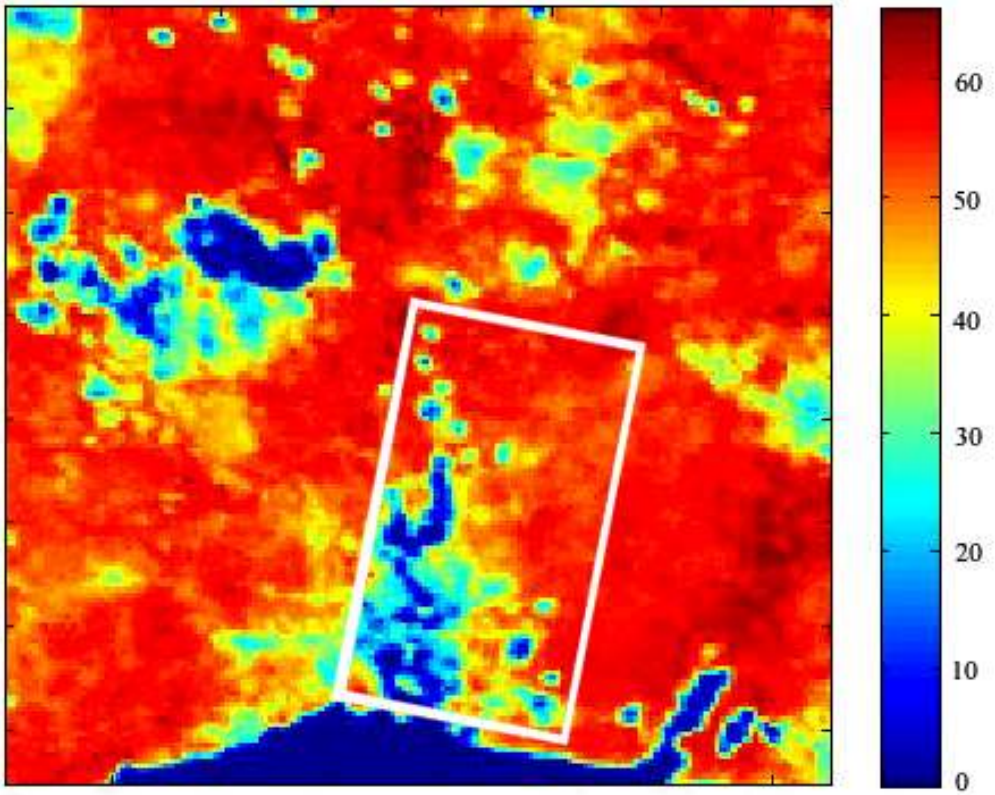

Figure 4.4 Spatial frequency of cloud free conditions on the month of December within an area of Bangkok metropolitan from 2006 - 2009.

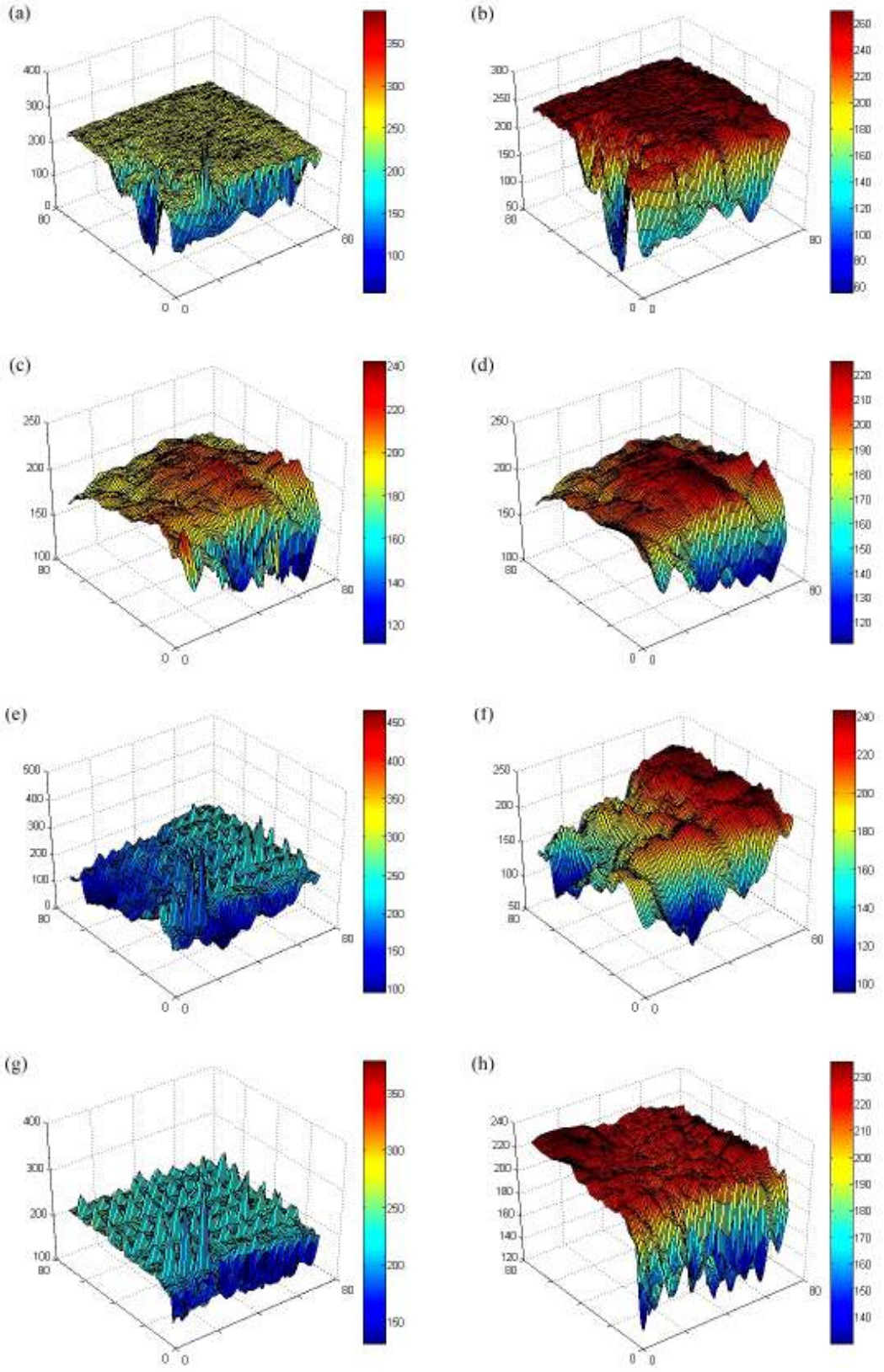

Figure 4.5 (left column) MODIS-ZWD data before the scan line correction, (right column) MODIS-ZWD data after the correction.

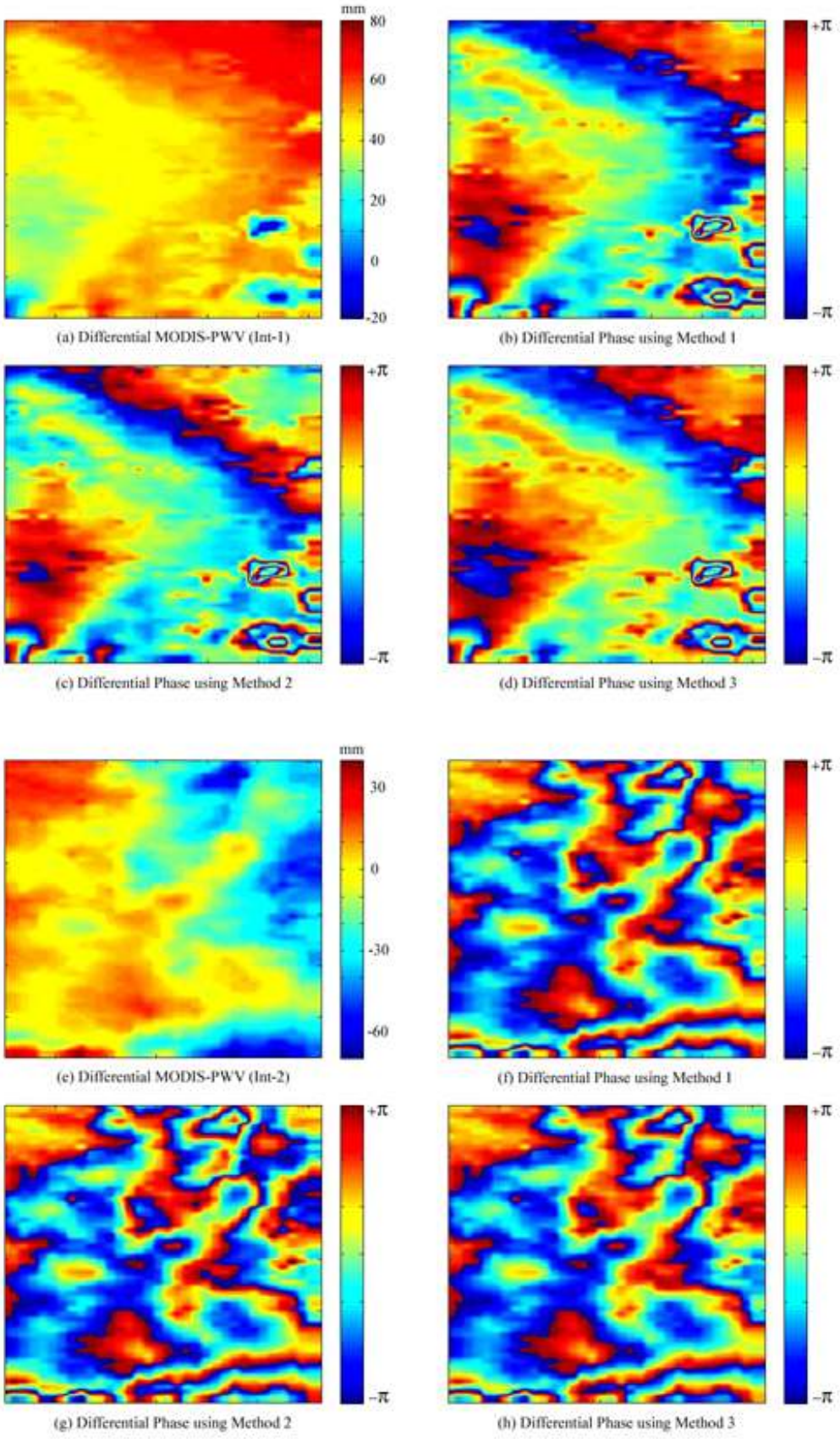

Figure 4.6 Differential MODIS-PWV data after converted into phase for water vapor correction in interferograms-1 and interferograms 2

4.3 Interferogram formation

Since SAR interferometry only works under coherent conditions, where the received reflections are correlated between the two SAR images. This implies that for every interferogram, changing reflection characteristics in time within a resolution cell should be avoided (Hanssen, 2001); the degree of interferometric correlation between the images is known as coherence. After the calculation and topographic phase removal of the interferograms, a number of output products were generated. Figure 4.7 showed the coherence of the phase of the interferograms. The coherence is a value between 0 and 1, representing the magnitude of decorrelation, hence coherence is a good measure of the phase information. From the study of Usai (1999) who found that for the retrieval of deformation in highly decorrelated interferograms by choosing a coherence threshold higher than 0.5, there was no significant improvement of the correlation coefficients between deformations retrieved from interferogram and from subsidence model, such that, in this study coherence threshold of 0.5 was set as minimum in order to analyze correlated phase pixel values. Geo-coded interferograms-1 and 2 after filtering were shown in figure 4.8a, 4.8b. Radar coordinated interferograms which were used for the water vapor correction were shown in figure 4.9 (top left).

It should be noted that lowest coherence values (darkest tones) corresponded both to agricultural area and water area (e.g. ponds) while the bright tones represented high coherence area which usually urban area consisting of permanent structure such as buildings, roads, bridges.

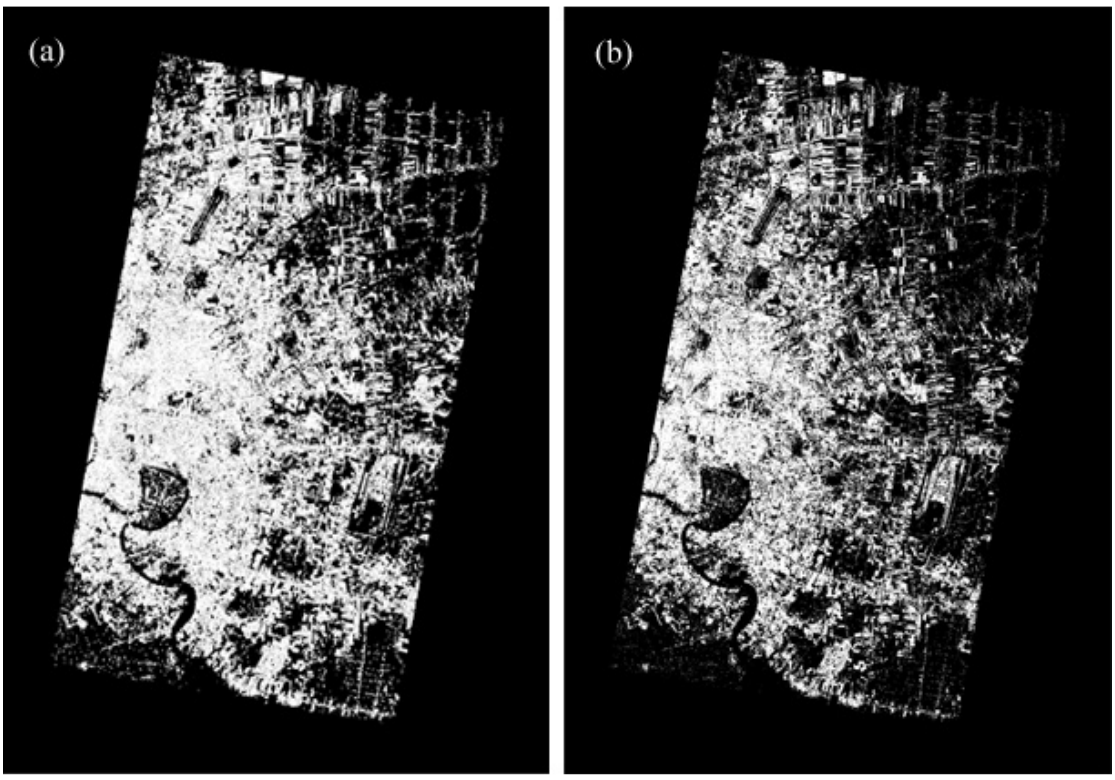

Figure 4.7 (a) the coherence map (threshold > 0.50) of interferogram-1 (white color represents high coherence area), (b) the coherence map of interferogram-2

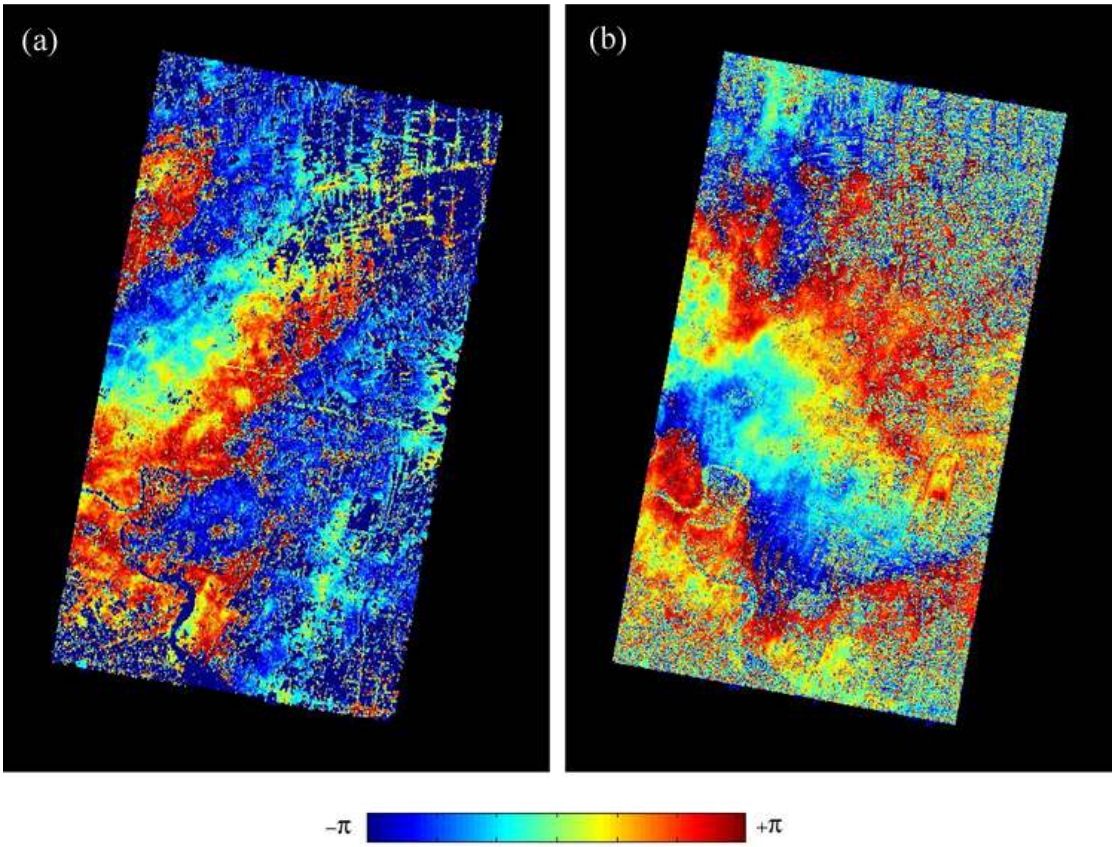

Figure 4.8 (a) interferogram-1shown in geographic coordinate after topographic removal (Oct 30, 2009 – Nov 21, 2000), (b) interferogram-2 after topographic removal (Dec 2, 2009 – Dec 24, 2009)

The differential phase had been unwrapped and transformed into height change value as shown in figure 4.11a, 4.13a. It should be noted that in this study: (1) the unwrapped phase had been converted to range change in millimeters and positive range change means atmospheric delay effect while some very small amount (less than 5%) of negative range change was due to phase unwrapping error; and (2) the unwrapped phase had been shifted by using a ground control points which was previously generated based on high coherence pixel (assumed no displacement) which was at the same location of unwrapped phase that represents the lowest delay.

From statistical point of view show that the maximum magnitude of the atmospheric effects from both unwrapped interferograms were up to 80 mm and mean values of 26.2 and 18.3 mm respectively as shown in table 4.3. It should be noted that the negative values in unwrapped interferogram resulting from phase unwrapping errors. From both interferogram-1 and interferogram-2 showed strong atmospheric phase effects that were not related to topography since baseline are small and the area is very flat). The patterns were the combination of several 100 meters up to many kilometers as seen on figure 4.9 (a) and 4.9 (e).

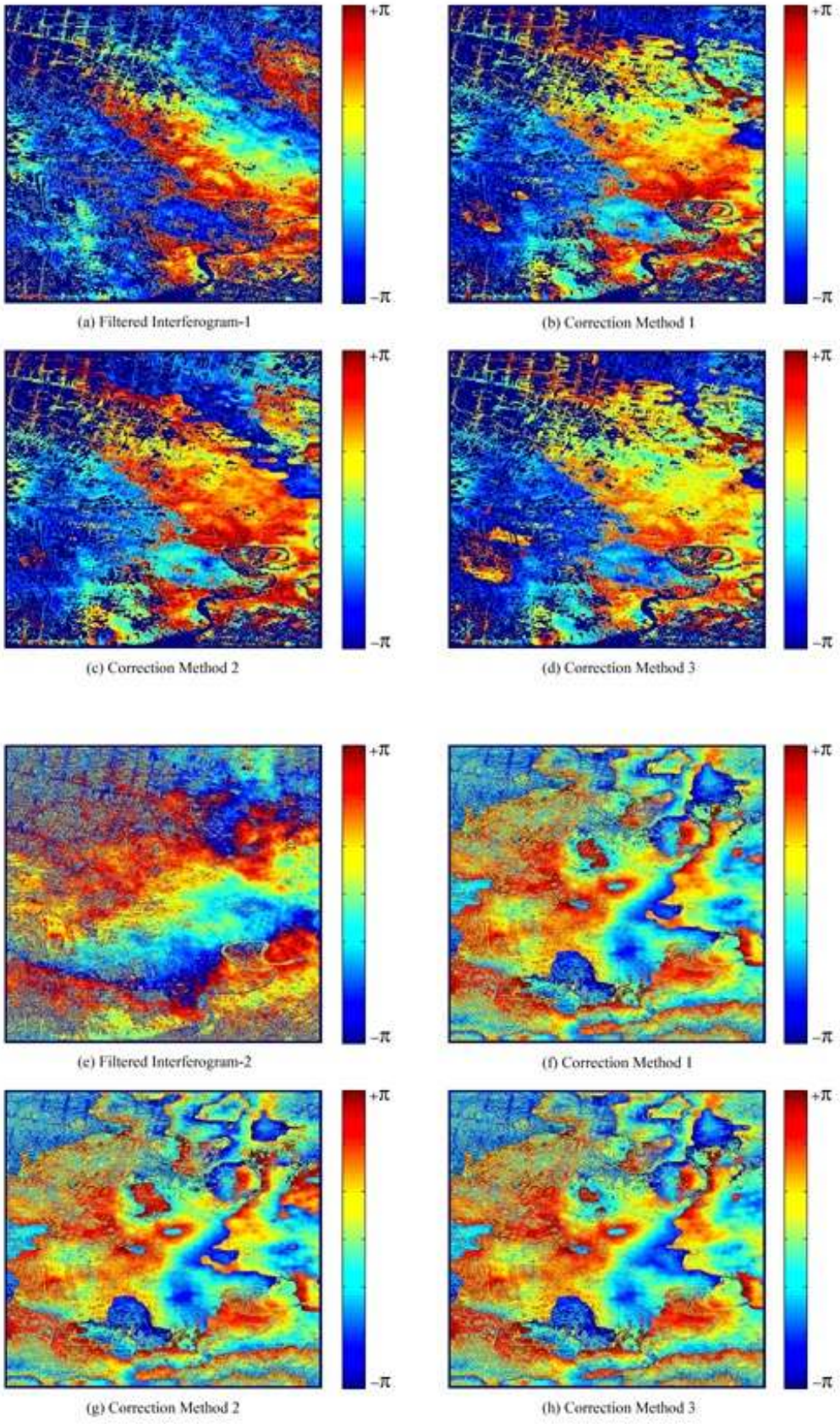

Figure 4.9 Results after applying differential phase converted from MODIS-ZWD in interferograms-1 and interferograms 2

4.4 The Correction results

Local atmospheric model for conventional repeat-pass SAR interferometry had been created and validated based on number of differential phase delay pixel values closer to zero. Since the calibration process was aimed to improve the model's ability for local water vapor correction which was tested in three different methods by means of improving correction locally from the least to the most; (1) without correction, (2) ground-based correction and (3) time-based correction. While the first scenario was used as a base case from which nothing had been improved, discussions were focusing on the validation of the latter two improving methods.

The TerraSAR-X interferogram-1 (October 30, 2009 – November 21, 2009) and 3 different atmospheric-corrected scenarios over Bangkok were shown in figure 4.11(a, b, c, d). It was observed that correction method 3 (figure 4.11d) provided the best result since the large phase delays (shown in brown color) around 30-40 mm were largely removed, leaving lower phase delay value in the corrected interferogram. In figure 4.10 (a, b, c, d), the histogram plots of the interferogram and its atmospheric corrected versions showed bi-modal distribution. It could be clearly seen that pixels of interferogram corrected by method 3 had the main peak near zero and the other peak at around 20, both of which moved towards the ideal pixel value of zero. However, a small percentage of pixels, especially those in the south-eastern part area, were over-corrected. Overall results showed that the correction method 1 and 2 were indifferent while method 3 gave better results with all the lower statistic values such as mean, mode except that of RMSE which was similar to the other two methods (table 4.4). Histogram of correction method 1 and 2 also gave a much higher number of pixels in lower range of phase delay values (around 0-20 mm) when compared with the non-corrected interferogram.

The results from interferogram-2 (2 December 2009 - 24 December 2009) were shown in 4.13(a, b, c, d) and the histogram plots were shown in 4.10 (e, f, g, h). The correction patterns were similar which the phase delays in dark yellow color around 10-20 mm were largely removed in the north-eastern part and the center area of the interferogram-2 (figure 4.13b, c, d). The main improvement from applying atmospheric correction was that more pixels were moved towards the ideal value of zero, resulting in higher pixel numbers of low values and smaller count of high values. However, certain pixels had larger delays as unlike the case of interferogram-1; however, no significant difference between different correction methods was observed. As all statistics such as mean, mode and RMSE were similar in all cases (table 4.4). It could also be noted that RMSE was not a sufficient indicator if phases in the interferogram were less fluctuated than the water vapor data which results in a higher RMSE even though there were more pixels with lower delay value within the interferogram after the correction.

Table 4.4 Results statistics of phase delay in mm. of both interferogram with 3 corrected scenarios. Statistics are calculated within a coherence threshold of > 0.5.

Interferogram	Method	Min	Max	Mean	Mode	RMSE
1	non-correction	-34.5	78.5	26.2	22.6	13.5
	method 1	-34.6	86	23.7	18.3	11
	method 2	-32	73.6	22.9	18.6	10.7
	method 3	-72	61.7	5.9	6.0	11.1
2	non-correction	-28.2	79.3	18.3	12.5	8.6
	method 1	-61.4	76.2	15.7	10.6	10.3
	method 2	-62.2	79.5	15.7	15.8	10.6
	method 3	-76.2	79.5	15.1	10	10.1

Table 4.5 Results statistics of pixels in each correction method after differentiated with the non-corrected interferogram.

Interferogram	Method	Lower delay	Indifference	Higher delay	total pixel
1	method 1	452,556	3,861	181,314	637,731
	method 2	478,454	3,796	155,481	637,731
	method 3	634,833	69	2,829	637,731
2	method 1	412,321	2,253	351,365	765,939
	method 2	438,517	2,311	325,111	765,939
	method 3	431,493	2,786	331,660	765,939

4.5 Discussions

Discussions can be divided into 4 different topics including the calibration results, the correction results, spatial characteristics of the differential interferogram and validation on using the simple mapping function.

4.5.1 The calibration results

For method 2, the ground-based calibration and correction results could be compared with the works by Li, *et al.,* (2005), who is the first to use MODIS water vapor data products in correcting the atmospheric phase delay in SAR interferogram but, all of his correction results were validated based on ERS data and calibrated with a dense GPS network data (Li, *et al.,* 2003a; Li, *et al.,* 2003b; Li, *et al.,* 2004; Li, *et al.,* 2005). In term of the calibration results, it showed that there were good linear relationships between ZWD_{MODIS} and the ZWD_{SAAS} value computed from the Saastamoinen model. The ZWD_{MODIS} appeared to overestimate the ZWD value against ZWD_{SAAS} with scale factors from 0.95 to 1.21. This was in accordance with the study by Li *et al*. (2003b) who found that MODIS-PWV overestimated PWV against GPS with scale factors from 1.07 to 1.14. It was also found that the ZWD_{MODIS} appeared to overestimate the ZWD_{SAAS} with 2 out of 3 stations (67%). This was in accordance with the study by Li *et al*. (2003b) who found that PWV was overestimated against GPS from 68 out of 86 or 79% of all tested GPS stations.

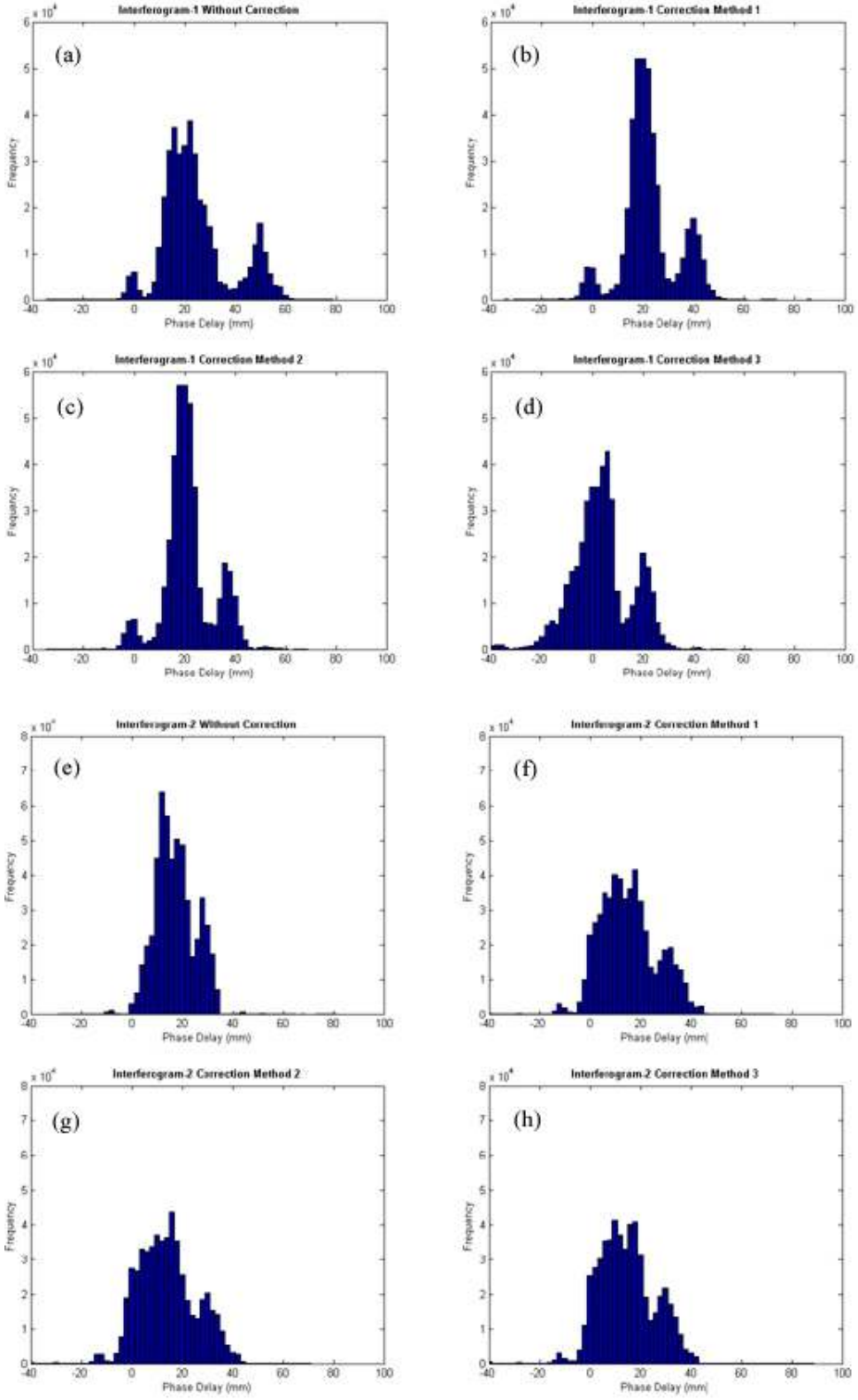

Figure 4.10 Histogram of interferogram-1 consisted of the interferogram without atmospheric correction (a) and three corrected scenarios using method 1, 2 and 3 respectively (b), (c), (d) and histogram of the interferogram-2 arranging in the same order as in interferogram-1(e), (f), (g), (h). Pixels plotted in all histogram were selected within a coherence threshold of > 0.5

4.5.2 The correction results

Differential interferogram produced from TerraSAR-X were acquired 22 days apart, there were 2 validation approaches both rmse and amount of lower delay pixels (from correction) used for the correction validation in this thesis.

For the validation comparing the rmse, in case of correction results as firstly reported by Li, *et al.,* (2003a), it was found that the differences of path delays with ERS data varied from -68 mm to 46 mm similar to result experimented on TerraSAR which varied between -32 mm to 73 mm and -62 mm to 79 mm (table 4.4). Similar to the results of the difference map between method1 – method 2, it was found that there was an increasing number of pixels with higher delay or a decreasing in delay values when applied correction method 2 (table 4.5). However, phase variation of the unwrapped interferogram in Li, *et al.,* (2005) decreased significantly from 2.48 radians to 1.47 radians after the correction. The correction results found in the interferogram-1 of this study was found to be 2.74 radians (13.5 mm) before correction and decreased to 2.17 radians (10.7 mm) after correction. Hence, it could be concluded that from the study, the result of interferogram-1 was in accordance with Li, *et al.,* (2005) while interferogram-2 in contrast, gave worse correction result with the increasing RMSE from 1.74 radians (8.6 mm) to 2.14 radians (10.6 mm). This might due to the density and water vapor variation within a day from both cases. The SCIGN region, California which appeared to have a very dense GPS networks with less water vapor amount than 40 mm as reported in the study of Li, *et al.,* (2005), while water vapor in Bangkok metropolitan on the date of correction was found to reach the maximum of 80 mm as seen in figure 4.6(a).

For method 3, the time-based calibration, the correction results were compared with the works by Li, *et al.,* (2006a), who first used MERIS water vapor data products in correcting the atmospheric phase delay in ENVISAT ASAR interferogram. The comparisons were made since MERIS and ASAR are acquired simultaneously during the day time which means there is no time difference gap between data issue such that were used to validate the time-based calibration method. The use of contemporaneous MERIS data to correct ENVISAT ASAR measurements showed a significant reduction in water vapor effects. There were two cases within SCIGN region in California where the unwrapped phase variations (RMSE) decreased from 2.38 radians before correction to 1.49 radians after correction which was similar to the results found in this study with 2.73 radians (13.5 mm) to 2.24 radians (11.1 mm) in interferogram-1. Unfortunately for the interferogram-2, the increasing RMSE from 1.74 radians (8.6 mm) to 2.04 radians (10.1 mm) was found. For the calibration purpose, the MERIS-PWV appeared to overestimate PWV against GPS under moderate condition with scale factors of 1.02 (Li, *et al.,* 2006b; Li, *et al.,* 2008) which was less than the range of scaling factors in MODIS case (1.07 to 1.14). The results from time-based calibration seemed to be in accordance with Li, *et al.,* (2006b) since the scaling factor of time-based calibration which were less than 1 (0.886 to 0.924) tend to decrease the ground-based calibration values as well (figure 4.1 and table 4.2).

Another way to validate the correction results was to create the different map comparing each method with the original unwrapped interferograms. The more correction values closer to zero, implied that the MODIS correction was effective (Li, *et al.,* (2004). From table 4.5, the pixels in differential map which gave value > 0

which mean the method lowered the phase delay or improved the interferogram, while pixels with gave value < 0 which mean the method added more delay (errors) to the original interferogram. Statistics were calculated within a coherence threshold of > 0.5. Overall correction results showed that, with the calibration of MODIS data gave better results when compared with the non-calibrated one. From the differential map between the non-correction one and each correction method (figure 4.12, 4.14), correction with method 3 gave the best results when compared with the increasing amount of lower delay pixels (table 4.5), but, also it gave the most errors (negative pixels) from over-correction (figure 4.11d). The method 1 and 2 however, almost give indifferent results which was conflicting with what reported in Li *et al.* (2005). This may due to the number of reference stations used in which in Li's number of GPS stations varied from 72-90 or an average of 80 over the SCIGN region which covered the area around 22,500 km^2 (Li *et al*., 2004) or the density of 1 GPS station per 280 km^2 compared to only 3 meteorological stations within 1,500 km^2 or 1 station per 500 km^2 in this research.

4.5.3 Spatial characteristics

In term of spatial analysis of the resulting interferograms, as Hanssen (2001) reported three regimes of atmospheric delay in interferograms (regime I: >2 km; regime II: 0.5–2.0 km; and regime III: 0.01–0.5 km). It showed that on average, atmospheric effects with wavelengths larger than the size of the interferogram (~30 km – regime I) could be reduced, while those with wavelengths shorter than the size of the interferogram (regime II, III) could not be effectively corrected and left with the atmospheric ripples which were still presented in the water vapor corrected interferograms. One possible reason which gave the correction results in interferogram-1 better than interferogram-2 was the different in spatial variation of MODIS-PWV data (figure 4.6a). Since both interferogram after the topographic phase removal produced a relatively smooth atmospheric phase variation. With a spatial smoothness of MODIS water vapor data similar to that spatial smoothness of atmospheric phase in the interferogram-1, the overall results were better.

Also, the IDW interpolation which produced a smooth surface, tend to have an effect with the smooth surface more than the fluctuated one, in this case it benefit more for MODIS data applied for interfergram-1 with a smoother surface. When compare between methods, which the correction result in method 3 was better significantly in term of phase delay reduction. It was found that the calculation of phase delay differs significantly (from π to $-\pi$); even from a slightly change of water vapor data if within a smooth surface. From the study, it could be concluded that other than that of correction approaches, the spatial variations of water vapor data used in the model was crucial, with large spatial variations of data used, the result could be more promising, while water vapor data with small spatial variations tend to add extensive errors to the original interferograms (figure 4.6e).

It was useful to note that, some characteristics of differential interferograms before correction might have a significant results from applying the water vapor product. due to the different in acquisition period season (at transition period) with a very different water vapor content, since the interferogram-1 was acquire during rainy season in Thailand, there should be large amount of water vapor during the time of acquisition hence, within the interferogram. Also, from theoretical studies as reviewed

within section 2.3, showed that the sensitivity of the tropospheric refractivity is highest for spatial variation in water vapor content (relative humidity), between 4 and 20 times greater than for temperature variation (Hanssen, 2001). Therefore, interferogram-2 which acquired during winter season, even there was less temperature which should increase the delay in the interferogram but, with less humidity during winter time, resulting in less water vapor induced within the interferogram. The consequence was that when applying the MODIS water vapor to each interferogram which had different amount of water vapor contents, the resultants of corrected interferogram were noticeably different and can be concluded that with more water vapor content within the interferogram (such as in interferogram-1 which acquired during rainy season), the better correction result. While the less water vapor content showed sign of over-corrected since there was very little that existed within the interferogram (such as in interferogram-2 which acquired during winter season).

4.5.4 Mapping function

In order to compute tropospheric delays at a certain elevation angle, or slant path delays. The simplest mapping function used in this modeling which is based on plane-parallel refractive medium (Li, 2005). There are numbers of more elaborate mapping functions e.g. Davis *et al.* (1985), Niell (1996; 2000) and Ifadis and Savvaidis (2001) which of these either use site location and surface meteorological data or only site location and time of year (Li, 2005). Li (2005) had tested the relative difference between using the simple mapping function and Niell Wet Mapping function at the HERS IGS GPS station at the latitude of 50.9 ^{o} and found that the relative difference was only 0.1% at the a view zenith angle of 23 ^{o} (or 67 ^{o} elevation angle). The result indicated that the simple mapping function could be used at a low view zenith angle (or at high elevation angle e.g. in this case of TerraSAR-X elevation angle between far ranges (65 ^{o}) and near range (62 ^{o}).

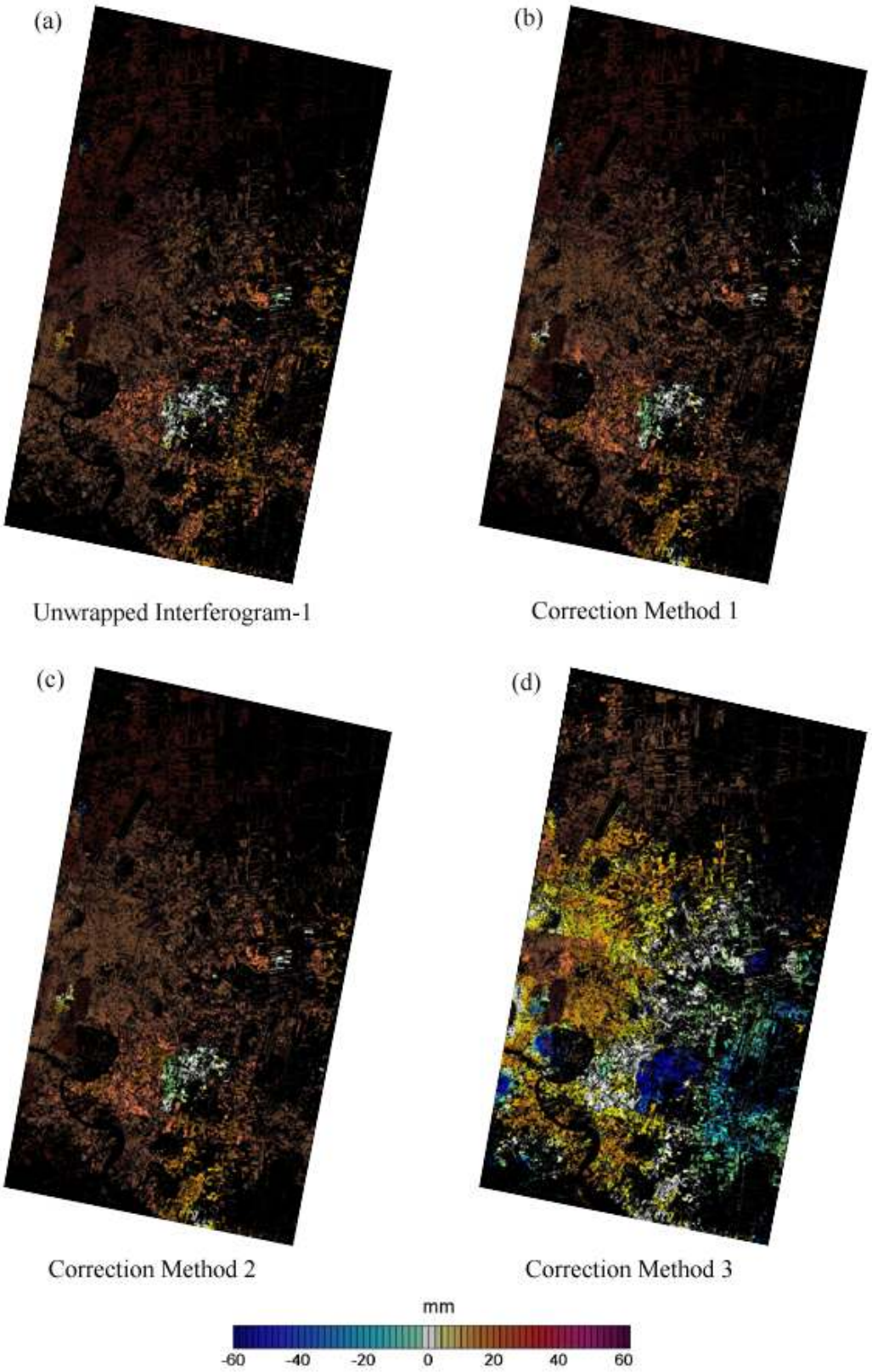

Figure 4.11 Unwrapped interferogram-1 (30 October 2009 - 21 November 2009) and 3 correction scenarios, only pixels with a coherence threshold of > 0.5 were considered in phase unwrapping.

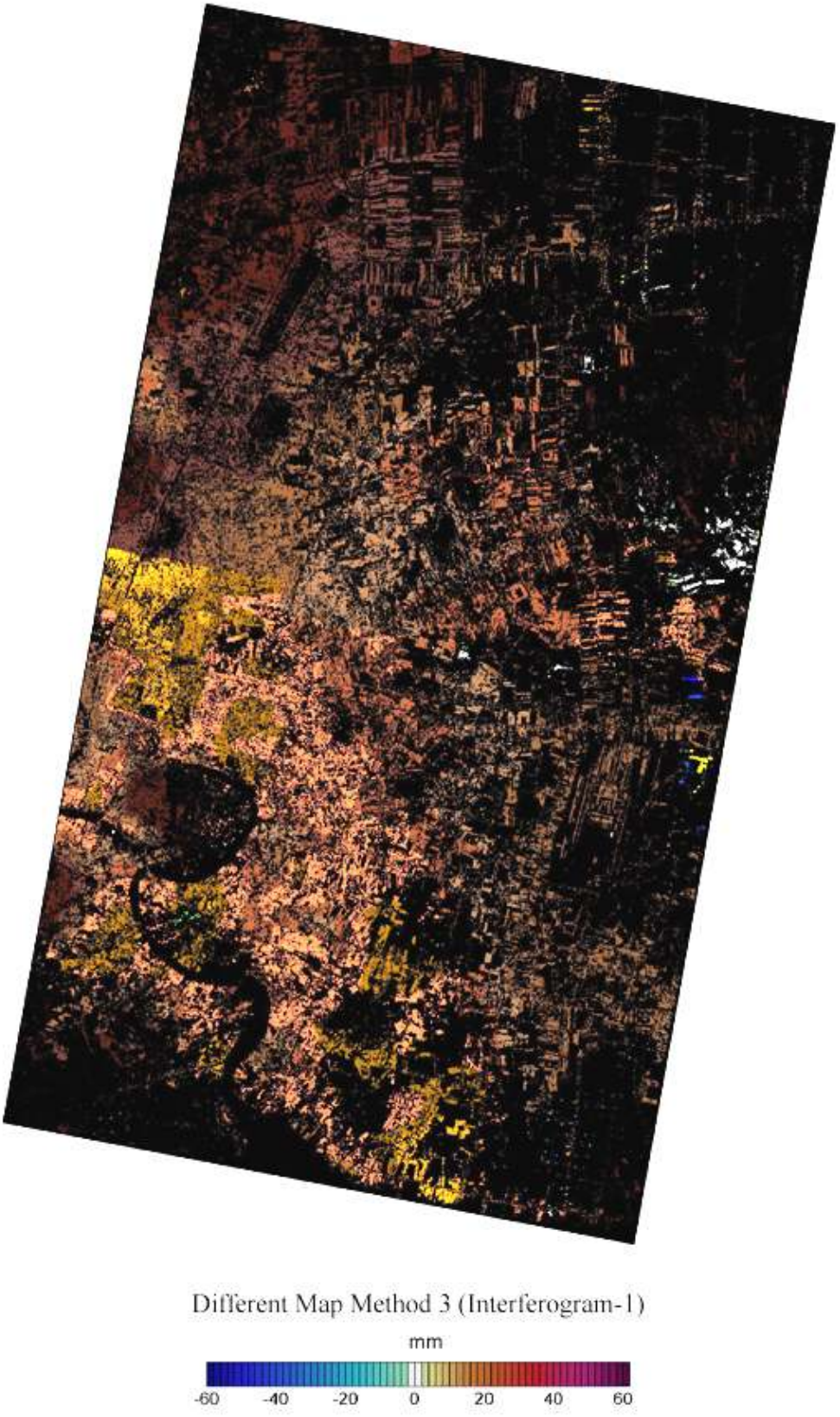

Figure 4.12 Different map between the original unwrapped – correction method 3 of interferogram-1 (30 October 2009 - 21 November 2009)

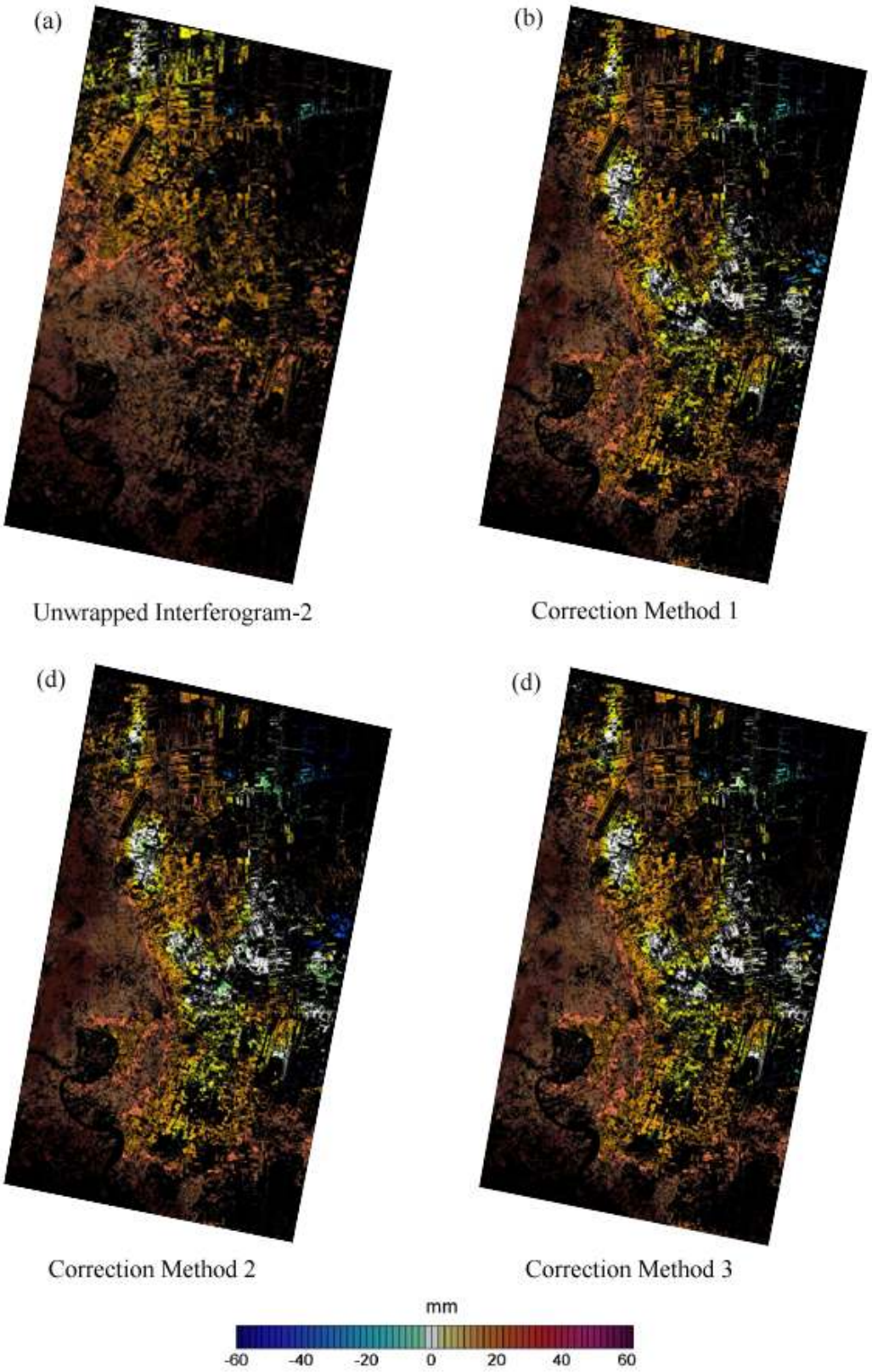

Figure 4.13 Unwrapped interferogram-2 (2 December 2009 - 24 December 2009) and 3 correction scenarios, only pixels with a coherence threshold of > 0.5 were considered in phase unwrapping

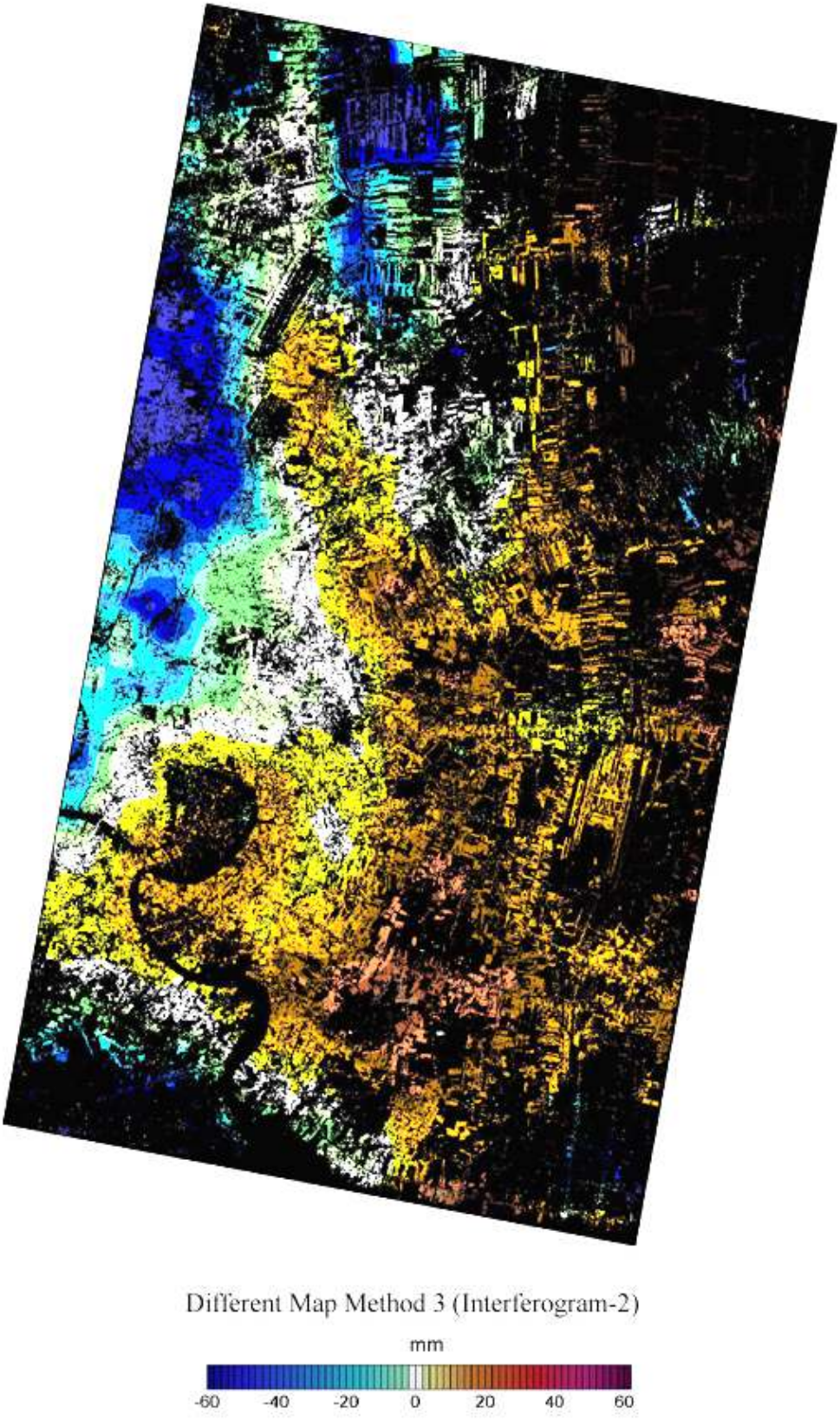

Figure 4.14 Different map between the original unwrapped – correction method 3 of interferogram-2 (2 December 2009 - 24 December 2009)

Chapter 5

Conclusion

5.1 Conclusions

In this thesis, local atmospheric model for conventional repeat-pass SAR interferometry has been created. The model was developed based on the integration of multi-station ground-based meteorological and MODIS water vapor data. The water vapor product from MODIS was processed to produce a zenith wet delay (ZWD) different maps while ground-based meteorological data was used for a calibration purpose. The calibration process aimed to improve the model's ability for local water vapor correction which was tested in three different scenarios based on degree of local corrections. The results were presented and validated based on number of differential phase delay pixel values close to the expected value of zero. It was found from the study that estimation of phase delays from MODIS improved by calibrating them with ground meteorological data. The calibration results showed that there were good linear relationships between MODIS-ZWD and the Saastamoinen model-ZWD even though the MODIS-ZWD appeared to be overestimated with the ones computed from the model. Since the ZWD estimated from these two sources were consistent thus, it was proposed to integrate Saastamoinen model and MODIS data for InSAR atmospheric correction. In this research, it was found that water vapor data with less spatial variations gave better atmospheric correction results. The 5 hour time-shifted linear fit models along with the IDW interpolation showed that there was a significant improvement on atmospheric phase delay correction using MODIS water vapor product.

5.2 Contribution of this research

The principle contributions of this research is the *Time-shifted linear model* which has been developed to improved time-difference aspect of MODIS water vapor correction to InSAR with a spatial resolution of 1 km x 1 km and successfully inserted within the InSAR processing steps. The extensive comparisons between MODIS-ZWD and ZWD computed from Saastamoinen model had been performed both in time and space and for the first time a meteorological data has been used to compare and calibrate with MODIS-ZWD. This can be the possible alternative tool in case the more accurate validation tool such as GPS is not available.

Recently, a well known Permanent Scatterers (PS) InSAR technique (PS-InSAR) which is a multi-image algorithm for conventional D-InSAR analysis aimed at extracting surface deformation measurement on a sparse grid of coherent radar targets. However, in order to perform in-depth studies of deformation phenomena, atmospheric signal is estimated and removed using atmospheric phase screen (APS) technique. A shortcoming of the method is that a significant number of SAR images over the same area, typically over 30 SAR images are needed to get reliable results (Hooper *et al.* 2004). Also, PS-InSAR is more suitable for slow-varying deformation phenomenon such as land subsidence, inter-seismic or post-seismic motion. The

conventional 2-pass D-InSAR technique on the other hand, has the advantage of requiring only two spatially coherent SAR images. Therefore, for abrupt change such as land slide or co-seismic motion, a 2-pass D-inSAR is more suitable. Also, using the technique, there is a specific need for tropical area since assumptions adopted in majority of 2-pass D-InSAR works in temperate area and desert or semi-desert may not be valid in tropical zone.

5.3 Recommendations for future research

Even though from the calibration results it was found that there were good agreements between ZWD computed from Saastamoinen model and MODIS-ZWD. However, the main problem was that, ZWD computed from the Saastamoinen model had poorer accuracy as mentioned in Li *et al.,* (2004b) which the rmse values of the Total Zenith Delay (TZD) models based on both the CGPS and ground meteorological observations was found to be around 0.5 cm while that based on ground meteorological observations only was over 4 cm. Therefore, the accuracy of the calibration process should be further improved if GPS were integrated in the model and if more GPS and ground meteorological stations are available. Also, as the availability of cloud-free MODIS data is limited, focus on further investigation is on the derivation of phase delay without MODIS from combination of GPS and meteorological data and the required combined density of which that can provide reliable estimate of atmospheric phase delay. The existing and upcoming infrastructure of Continuous GPS (CGPS) networks will offer the great opportunity to further test seasonal and temporal water vapor variation. Future research should be able to monitor the water vapor characteristic both temporally and spatially in order to get more reliable parameters for tropospheric correction model.

5.4 Concluding remark

There has been a need for surface deformation study to remove atmospheric phase term from interferograms created by 2-pass DInSAR technique. This is especially the case when the area of interest is in tropical zone and the assumption adopted in many studies of arid or semi-desert areas that the atmosphereic phase term due to water vapor content is small comparing with the deformation signal may not be valid. The technique presented in this paper can be easily adopted for the estimation of phase delay. The MODIS water vapor measurements however, are sensitive to the presence of clouds and since the global average cloud free frequency is only 25% (Wylie and Menzel; Li *et al.,* 2009). From available 23 TerraSAR-X images in the archive, only 4 images were matched with the cloud free condition of MODIS-PWV data which means, the low frequency of cloud free observations could be a major limitation in applying MODIS near IR water vapor products to InSAR atmospheric correction. With more upcoming TerraSAR-X images, further research needs to be carried out to enhance the accuracy and reliability of the method.

REFERENCES

Aobpaet, A., Cuenca, M., Hooper, A., Trisirisatayawong, I. (2010). Land subsidence evaluation using InSAR time series analysis in Bangkok metropolitan area. *Fringe 2009 Workshop.* Frascati, Italy.

Bamler, R. (1999). The SRTM Mission: A World-Wide 30m Resolution DEM from SAR Interferometry in 11 Days. *Photogrammetric Week 1999.* Wichmann Verlag, Heidelberg: 145-154.

Bevis, M., Businger, S., Herring, T., Rocken, C., Anthes, R., & Ware, a. R. (1992). GPS meteorology: remote sensing of atmospheric water vapor using the Global Positioning System. *Journal of Geophysical Research , 97*: 15,787-15,801.

Bonforte, A. F. (2001). Calibration of atmospheric effect on SAR interferograms by GPS and local atmosphere models: first results. *J. Atmos. Terr. Phys.* , 1343-1357.

CREASO. (2007). *SARScape technical description*. [Online]. Available from: http://www.sarmap.ch/index.php [August 16, 2010]

Crosetto, M. C. (2002). Quantitative subsidence monitoring using SAR interferometry. *Geoscience and Remote Sensing Symposium, IGARSS '02. IEEE International.* , 1231-1233.

Ding, X. L. (2008). Review: Atmospheric Effects on InSAR Measurements and Their Mitigation. *Sensors* , 5426-5448.

Dzurisin, D. Z. (2007). Interferometric Synthetic Aperture Radar (InSAR). *Volcano Deformation: Geodetic Monitoring Techniques* .

Eineder, M. and Fritz, T. (2006). TerraSAR-X Ground Segment, SAR Basic Product Specification Document (TX-GS-DD-3302), Release 1.4, 06.

Emardson, T., Simons, M., & Webb, F. (2003). Neutral atmospheric delay in interferometric sysnthetic aperture radar applications: Statistical description and mitigation. *Journal of Geophysical Research 108*: 2231.

Farr, T. M. (2000). Shuttle Radar Topography Mission produces a wealth of data. *Amer. Geophys. Union Eos*, 583-585.

Ferreti, A., & Novali, F. P. (2005). Statistical analysis of atmospherical components in ERS SAR data. *Fringe'05.* Frascati, Rome.

Ferretti, A. C. (2001). Permanent Scatterers in SAR Interferometry. *IEEE Transactions on Geoscience and Remote Sensing* , 8-20.

Ferretti, A., Prati, C., & Rocca, F. (2000). Nonlinear Subsidence Rate Estimation Using Permanent Scatters in Differential SAR Interferometry. *IEEE T. Geosci. Remote Sensing* , 2202-2212.

Ferretti, A., Savio, G., Barzaghi, R., Borghi, A., Musazzi, S., Novali, F., et al. (2007). ubmillimeter Accuracy of InSAR Time Series: Experimental Validation. *Geoscience and Remote Sensing, IEEE* , 1142 - 1153.

Fruneau, B. S. (2000). Detection of ground subsidence in the city of Paris using radar interferometry: interferometry: isolation of deformation from atmospheric artifact using correlation. *Geophys. Res.Lett*, 3981-3984.

Galloway, D., & Hoffman, J. (2007). The application of satellite differential SAR interferometry-derived ground displacements in hydrogeology. *Hydrogeology Journal 15* (1): 133-154.

Gao, B. C., & Kaufman, a. Y. (2003). Water vapor retrievals using Moderate Resolution Imaging Spectroradiometer (MODIS) near-infrared channels. *Journal of Geophysical Research 108:* (D13, 4389).

Goldstein, R. (1995). Atmospheric limitations to repeat-track radar interferometry. *Geophys. Res. Lett.* , 2517-2520.

Hanssen, R. a. (1996). A first quantitative evaluation of the atmospheric effects on SAR interferometry and Sea Surface Images. *CEOS SAR Workshop*, (pp. 33-39). ESTEC, Noordwijk.

Hanssen, R. F. (1998). High-resolution water vapor mapping from interferometric radar measurements. *Science* , 1297-1299.

Hanssen, R. (2001). *Radar Interferometry: Data interpretation and Error Analysis*. Kluwer Academic Publishers: Dordrecht.

Hole, J. B. (2007). Subsidence in the geothermal fields of the Taupo Volcanic Zone, New Zealand from 1996 to 2005 measured by InSAR. *Journal of Volcanology and Geothermal Research* 125–146.

Janssen, V. G. (2004). Tropospheric correction to SAR interferometry from GPS observations. *GPS Solut* , 140-151.

Kampes, B. M. (2006). *Radar Interferometry: Persistent.* Springer.

Katsougiannopoulos, S., Pikridas, C., Rossikopoulos, D., Ifadis, I. M., & Fotiou, a. A. (2006). Tropospheric Refraction Estimation Using Various Models,

Radiosonde Measurements and Permanent GPS data. *XXIII FIG Congress*. Munich, Germany.

Kos, T., Botincan, M., & Markezic, I. (2008). Estimation of Tropospheric Delay Models compliance. *50th International Symposium ELMAR-2008*. Zadar, Croatia.

Li, Z. M. (2003a). Tropospheric correction techniques in repeat-pass SAR interferometry. *Proceedings of the Fringe 2003 workshop, ESA ESRIN*. Frascati, Italy.

Li, Z. M. (2003b). Comparison of precipitable water vapor derived from radiosonde, GPS, and Moderate-Resolution Imaging Spectroradiometer measurements. *Journal of Geophysical Research , 108*.

Li, Z. (2004a). Production of regional 1 km x 1 km water vapor fields through the integration of GPS and MODIS data. *Proceedings of the 17th International Technical Meeting of the Satellite Division of The Institute of Navigation.* Long Beach, California, USA.

Li, Z., Ding, X., & Liu, G. (2004b). Modeling atmospheric effects on InSAR with meteorological and continuous GPS observations: algorithms and some test results. *Journal of Atmospheric and Solar-Terrestrial Physics , 66*: 907–917.

Li, Z. (2005). Modeling atmospheric effects on repeat-pass InSAR measurements. Ph.D Dissertation, the Hong Kong Polytechnic University, Hong Kong

Li, Z., Muller, J., Cross, P., & Fielding, a. E. (2005). Interferometric synthetic aperture radar (InSAR) atmospheric correction: GPS, Moderate Resolution Imaging Spectroradiometer (MODIS), and InSAR integration. *Journal of Geophysical Research 110*.

Li, Z., Fielding, E. J., Cross, P., & Muller, a. J. (2006a). Interferometric synthetic aperture radar atmospheric correction: Medium Resolution Imaging Spectrometer and Advanced Synthetic Aperture Radar integration. *Geophys. Res. Lett , 111*.

Li, Z., Muller, J.-P., Cross, P., Albert, P., Fischer, J., & Bennartz, a. R. (2006b). Assessment of the potential of MERIS near-infrared water vapour products to correct ASAR interferometric measurements. *International Journal of Remote Sensing , 27* (2): 349-365.

Li, Z. (2008). Reduction of atmospheric water vapor effects on Envisat ASAR interferograms using MERIS Near IR measurements. *The XXI Congress of the International Society for Photogrammetry and Remote Sensing*. Beijing, China.

Li, Z. F. (2009). Advanced InSAR atmospheric correction: MERIS/MODIS combination and stacked water vapour models. *International Journal of Remote Sensing* , 3343-3363.

Massonnet, D. F. (1995). Discrimination of geophysical phenomena in satellite radar interferograms. *Geophys. Res. Lett* , 1537-1540.

Massonnet, D. a. (1998). Radar Interferometry and Its Application to Changes in the Earth's Surface. *Rev. Geophys* , 441-500.

Mendes, V. (1999). Modeling the neutral-atmosphere propagation delay in radiometric space techniques. *Doctoral Dissertation*. New Brunswick, Canada: University of New Brunswick.

Phienwej, N. G. (2006). Bangkok Land Subsidence. *Engineering Geology , 82* (4): 187-201.

Poncos, V., & Dana, I. (2008). Interferometric Generation of Digital Elevation Models for Urban Areas Using TerraSAR-X.

Price, E. J. (1998). Small-scale deformations associated with the 1992 Landers, California, earthquake mapped by synthetic aperture radar interferometry phase gradients. *J. Geophys. Res*. 27001-27016.

Qu, W.-J., Zhu, W.-Y., Song, S.-L., & Ping, J.-S. (2008). Evaluation of the Precision of Three Tropospheric Delay Correction Models. *Chinese Astronomy and Astrophysics , 32* (4): 429-438.

Rabus, B. E. (2003). The shuttle radar topography mission—a new class of digital elevation models acquired by spaceborne radar. *Journal of Photogrammetry and Remote Sensing* 241−262.

Raucoules, D. C. (2007). Use of SAR interferometry for detecting and assessing ground subsidence. *Compt. Rend. Geosci.* , 289–302.

Saastamoinen, J. (1972). Atmospheric correction for the troposphere and stratosphere in radio ranging of satellites. *Geophysics monograph 15, 3rd Int. Symp. Use of Artificial Satellites for Geodesy, AGU*: 247-251.

Sarti, F. V. (1999). A method for the automatic characterization of atmospheric artifacts in SAR interferograms by correlation of multiple interferograms over the same site. *Proceedings of IGARRS'99.* Hamburg, Germany.

Sarti, F., & Fruneau, B. C. (2000). Isolation of atmospheric artifacts in differential interferometry for ground displacement detection: comparison of different methods. *Proceedings of the European Space Agency ERS-Envisat Symposium.* Gothenburg, Sweden.

Shepard, D. (1968). A two-dimensional interpolation function for irregularly-spaced data. *Proceedings of the 1968 ACM National Conference* , 517–524.

Tarayre, H. a. (1996b). Atmospheric propagation heterogeneities revealed by ERS-1 interferometry. *Geophysical Research Letters* , 989–992.

Tarayre, H. a. (1996a). Atmospheric artefacts on interferograms. *Proc. FRINGE 1996*, (pp. 125-128). Zurich, Switzerland.

Tarayre, H., & and Massonnet, D. (1996). Atmospheric artefacts on interferograms. *Proc. FRINGE 1996*: 125-128.

Tarayre, H., & and Massonnet, D. (1994). Effects of a Refractive Atmosphere on Interferometric Processing. *Proceedings of IGARSS '94*, (pp. 717-719). Pasadena, California.

Usai, S. a. (2000). On the interferometric characteristics of anthropogenic features. *Geoscience and Remote Sensing, IEEE Transactions* , 1734-1736.

Webley, P. B. (2002). Atmospheric water vapour correction to InSAR surface motion measurements on mountains: results from a dense GPS network on Mount Etna. *Phys. Chem. Earth* , 363-370.

Wegmuller, U. C. (2006). Ionospheric electron concentration effects on SAR and InSAR. *IGARSS 2006. IEEE International Conference*, 3731 – 3734.

Williams, S. Y. (1998). Integrated satellite interferometry: Tropospheric noise, GPS estimates and implications for interferometric synthetic aperture radar products. *J. Geophys. Res.* , 27: 051–27,067.

Zebker, H. A., Rosen, P. A., & Hensley, S. (1997). Atmospheric effects in interferometric synthetic aperture radar surface deformation and topographic maps. *Journal of Geophysical Research , 102*: 7547-7563.

Zhou X., C. N.-B. (2009). Applications of SAR Interferometry in Earth and Environmental Science Research. *Sensors. 2009*: 1876-1912.

VITA

Graduated from the faculty of Architecture, Chulalongkorn University in 1999 and had been working as an assistant architect for 3 years before pursued study on Geographic Information Systems and Remote Sensing at Khon Kaen University. After graduated, continue PhD. study at the department of Survey engineering, Chulalongkorn University in 2007.